

Chapter II

**Multi-technique equation of state for Fe₂SiO₄ melt and the
density of Fe-bearing silicate melts from 0 – 161 GPa**

Claire W. Thomas

Qiong Liu

Carl B. Agee

Paul D. Asimow

Rebecca A. Lange

Accepted to

Journal of Geophysical Research

August 27, 2012

ABSTRACT

New equation of state measurements on liquid Fe_2SiO_4 have been conducted in a collaborative, multi-technique study. The liquid density (ρ), the bulk modulus (K), and its pressure derivative (K') were measured from 1 atm to 161 GPa using 1-atm double-bob Archimedean, multi-anvil sink/float, and shock wave techniques. Shock compression results on initially molten Fe_2SiO_4 (1573 K) fitted with previous work and the ultrasonically-measured bulk sound speed (C_o) in shock velocity (U_S)-particle velocity (u_p) space yields the Hugoniot: $U_S = 1.58 \pm 0.03 u_p + 2.438 \pm 0.005$ km/s. Sink/float results are in agreement with shock wave and ultrasonic data, consistent with an isothermal $K_T = 19.4$ GPa and $K' = 5.33$ at 1500°C. Shock melting of initially solid Fe_2SiO_4 (300 K) confirms that the Grüneisen parameter (γ) of this liquid increases upon compression where $\gamma = \gamma_o(\rho_o/\rho)^q$ yields a q value of -1.45 . Constraints on the liquid fayalite EOS permit the calculation of isentropes for silicate liquids of general composition in the multi-component system CaO-MgO-Al₂O₃-SiO₂-FeO at elevated temperatures and pressures. In our model a whole-mantle magma ocean would first crystallize in the mid-lower mantle or at the base of the mantle were it composed of either peridotite or simplified “chondrite” liquid, respectively. In regards to the partial melt hypothesis to explain the occurrence and characteristics of ultra-low velocity zones, neither of these candidate liquids would be dense enough to remain at the core mantle boundary on geologic timescales, but our model defines a compositional range of liquids that would be gravitationally stable.

INTRODUCTION

The formulation of an accurate equation of state (EOS) for silicate melts at high pressure and temperature is necessary to understand fully the important role of liquids in the differentiation and formation of terrestrial planets. The early history of the Earth may well have included one or more deep magma ocean events, perhaps extending to the core-mantle boundary (CMB) [Labrosse *et al.*, 2007]. During crystallization of magma oceans and also during partial melting events in predominantly solid mantle environments, the formation of chemically distinct reservoirs is controlled by gravitational differentiation and therefore intimately linked to the solid and liquid EOS. In particular, the possibility of crystal-liquid density cross-overs — that is, for a given liquid and a given mineral or assemblage of minerals, a horizon above which the liquid rises but below which it sinks [Agee, 1988; Stolper *et al.*, 1981] — implies dramatic bifurcation points in the possible paths of differentiation, leading to formation of either rising or sinking enriched reservoirs. These rising or sinking liquids will either potentially form crust or else potentially be sequestered at depth. Furthermore, changes in chemical equilibria with increasing pressure are defined by molar volume, the pressure derivative of the Gibbs free energy [Asimow and Ahrens, 2010]. Thus, accurate models of both the thermodynamic and fluid dynamic evolution of the Earth demand a fundamental knowledge of silicate liquid volumes at extreme pressure and temperature conditions.

In addition, detection of ultra-low velocity zones (ULVZ) [Garnero and Helmberger, 1995] at the base of the mantle may indicate the presence of silicate partial melts [Lay *et al.*, 2004; Mosenfelder *et al.*, 2009; Williams *et al.*, 1998] or more specifically iron-bearing melts [Labrosse *et al.*, 2007]. Seismic observations such as S- and P-wave speeds and inferred density have given clues as to the nature of the materials in ULVZs, but there are a number of candidate

iron-bearing solid phases that can produce the correct drops in wave speed and increased density without partial melting. Proposed phases include ferropericlase (Fe, Mg)O [Wicks *et al.*, 2010] and iron-enriched post-perovskite [Mao *et al.*, 2006]. Thus, improved constraints on iron-bearing silicate liquid densities at elevated pressure and temperature will aid in answering whether a liquid or liquid-solid mush could be dynamically stable at the CMB and similarly what the relative buoyancy of melt and its co-existing solids would be. There are presently no published experimental constraints on the density of iron-bearing silicate liquids beyond 47 GPa [Chen *et al.*, 2002; Miller *et al.*, 1991a].

Silicate liquids occupy a large, multi-dimensional continuum of compositions and therefore understanding their range of behavior requires either data on a very large number of compositions or data on a minimum set of end-member compositions and a reliable means of interpolating in composition space. At low pressure, ideal mixing of volumes has proven to be a reliable tool [Lange and Carmichael, 1987], but it remains poorly tested at high pressure [Asimow and Ahrens, 2010]. Here we present results on a pure iron-bearing end-member, fayalite (Fe_2SiO_4). In the future, this will allow assessment of intermediate compositions with lower iron contents without the need for extrapolation and provide an essential tie-point for the assessment of linear mixing along iron-magnesium mixing joins.

Previous shock experiments on fayalite (Fe_2SiO_4) liquid achieved pressures up to 47 GPa [Chen *et al.*, 2002], which corresponds to about mid-mantle range [Dziewonski and Anderson, 1981]. For this work, we extended this pressure range to 161 GPa, beyond CMB pressures, so we may apply our results to understanding the effects of iron on deep mantle systems. Additionally, this collaborative work sought to resolve inconsistencies in previous reports on Fe_2SiO_4 liquid compressibility and its change with pressure. Published isothermal static compression data from

sink/float experiments [Agee, 1992] and shock wave results [Chen *et al.*, 2002] are in close agreement for bulk modulus (K_0) values but differ greatly on the value of the pressure derivative (K'), 10.1 (isothermal) and 5.36 (isentropic), respectively, which give very divergent predictions for density at higher pressure. Isothermal and isentropic equations of state need not be the same, but a larger K' for the isotherm implies a negative coefficient of thermal expansion, which is contrary to expectations. The anomaly is even more apparent when the Hugoniot data at estimated shock temperatures are compared to the extrapolated isotherm (Figure 1). For instance, at 15 GPa, the estimated shock state is at temperature (T_S) 1783K and density $\sim 4.75 \text{ g cm}^{-3}$, somewhat denser than the extrapolated isotherm at the same P and T , $\sim 4.5 \text{ g cm}^{-3}$. At 50 GPa however, the estimated Hugoniot state is at temperature 2943 K and density $\sim 6.0 \text{ g cm}^{-3}$, much denser than the extrapolated 1773 K isotherm at 50 GPa, 4.75 g cm^{-3} , whereas one expects density to decrease with increasing temperature. This discrepancy was also noted by Ghiorso (2004), whose equation of state fitting exercise produced an internally consistent prediction of all fusion curve data and Hugoniot volume data, but underestimated the density of neutral buoyancy experiments from Agee [1992] by 1%.

We have conducted new measurements of the equation of state of molten fayalite (Fe_2SiO_4) using the following techniques: (i) double-bob Archimedean method for melt density and thermal expansion at ambient pressure (University of Michigan), (ii) multi-anvil sink/float technique to measure melt density to 4.5 GPa (University of New Mexico), and (iii) shock wave measurements of P - V - E equation of state to 161 GPa (Caltech). The aim of this multi-technique study has been to measure the density of molten Fe_2SiO_4 , to resolve the discrepancy in published EOS for this material, and to use the measured equation of state to address processes of early earth differentiation and stability of a liquid at the CMB.

METHODS

1- atm double-bob Archimedean methods

The shared starting material for the double-bob density measurements and the shockwave experiments was synthesized at the University of California, Berkeley, by Mark Rivers and contains 64.48 mol% Fe as FeO, 34.97 mol% SiO₂, and 0.56 mol% Al₂O₃ (wet chemical analysis is reported in *Rivers and Carmichael* [1987]), slightly off fayalitic composition (66.66 mol% FeO, 33.33 mol% SiO₂). This is the same material used for ambient ultrasonic sound speeds reported in *Ai and Lange* [2004].

The starting material was a brick-red powder with iron predominantly in the form of ferric iron (Fe³⁺). To produce a starting composition with iron as Fe²⁺, approximately 75 g was loaded step-wise in four batches (~18-20 g each) into a straight-wall molybdenum crucible (7.8 cm deep and 3.6 cm inner diameter) placed in a Deltech furnace at 1300°C in a reducing stream of 1%CO-99%Ar. Each batch of melt was held at 1300°C for 12 hours until all 75 grams were loaded into the crucible and reduced. The Mo crucible was then placed on a platform in the Deltech furnace such that the top 3 cm of the liquid corresponded with the isothermal hotspot in the furnace. A thermal profile from the top of the crucible down into the sample had been previously documented for a Mo crucible filled with alumina powder for each temperature of measurement. Temperature was measured at the top of the crucible with an S-type thermocouple, calibrated against the melting temperature of gold.

Liquid density measurements were made on the Fe₂SiO₄ liquid using the double-bob Archimedean method, described in detail in *Lange and Carmichael* [1987]. The method was adapted for a reducing atmosphere (1%CO-99%Ar) in this study by using molybdenum instead of platinum for the two bobs and the crucible. An electronic balance with a precision of ±0.0001

g was mounted on an aluminum platform above the furnace to measure the weights of the Mo bobs before and after immersion into the Fe_2SiO_4 liquid. By using two Mo bobs of different mass (~20 and ~7 g), but identical stem diameters (1 mm), the effect of surface tension on the stem was eliminated. The density of the liquid is calculated from the following equation:

$$\rho(T) = \frac{B_L(T) - B_S(T)}{V_L(T) - V_S(T)} \quad (1)$$

where $B_L(T)$ and $B_S(T)$ are the buoyancy of the large and small bob, respectively, and $V_L(T)$ and $V_S(T)$ are the immersed volume of the large and small bob, respectively. The buoyancy is defined as the mass of the bob in the gas stream (corrected to vacuum) minus the mass of the bob during the immersion in the Fe_2SiO_4 melt. Four density measurements were made at each temperature with two different large bobs and two different small bobs. The accuracy of using Mo bobs instead of Pt bobs was tested by measuring the density of NaCl liquid at 1286 K and the result (1.445 g/cm³) closely matches that recommended by NIST [Janz, 1980] at this temperature (1.441 g/cm³).

Sink/float methods

Fayalite used for sink-float experiments was the same sample used in the original Agee [1992] study. This is a different starting material than used in the double-bob density and shockwave measurements of this study. The fayalite was synthesized in a Deltech gas-mixing furnace for 24 hours at controlled $f\text{O}_2$ (IW-1). All sink-float experiments were carried out in a Walker-style multi-anvil device at the University of New Mexico, as opposed to a piston-cylinder device at the Bayerisches Geoinstitut used in Agee [1992]. Two types of gem-quality marker spheres were used: a spessartine garnet from the Malagasy Republic with composition $\text{Alm}_{10.6}\text{Sp}_{89.4}$ (also used in Agee [1992]) and a San Bernardino almandine-rich garnet

Alm_{80.0}Gr_{s8.9}Sps_{6.4}Pyr_{4.7}. Experiments were run in high purity molybdenum capsules, with run times of approximately 30 seconds at 1500°C. For further details of the experimental method, see *Circone and Agee* [1996].

Shock wave methods

Sample synthesis and preparation of preheated (1573 K) shots

The shared starting material used for the shock wave and double-bob experiments was reduced in a similar manner as described above in the double-bob methods section to produce a starting composition with the correct oxidation state (Fe²⁺). The powder was melted in a deep (3.5 cm deep, 1.7 cm inner diameter) molybdenum crucible hung on molybdenum wires in a Deltech furnace at 1300°C in a reducing gas stream of 1% CO-99% Ar. The powder was melted in short 30-45 minute runs; quenched and re-filled several times to reach the crucible's capacity; and then left to equilibrate for 18 hours at temperature. The quenching process used was unfortunately slow to avoid CO gas release or rapid oxidation on hot exposure to air. An extra-long ceramic hanging rod was used to push the crucible out of the hot spot to the bottom of the furnace tube to cool within the reducing atmosphere. Once the crucible was no longer glowing red (approximately 10 minutes), nitrogen was streamed for 10 minutes followed by a finishing quench in water. A combination of volume reduction on crystallization and surface tension at the crucible walls typically left a 5mm diameter triangular pit in the center, which reached nearly half way to the bottom of the crucible.

Mössbauer spectra measured by Bjorn Mysen at the Carnegie Institution of Washington confirmed that Fe in the run products was reduced and dominantly in the form of fayalite and wüstite (FeO) with minor amounts of an iron-bearing accessory mineral, most likely magnetite. This aggregate was too fragile to be lapped into disks to fit into shock wave experiment sample

holders, so it was re-ground and hot-pressed in a piston-cylinder device at 10 kbar and 725°C using a graphite sleeve and CaF₂ base plug. The maximum fO₂ in our graphite sample assembly is controlled by the CCO buffer [Holloway *et al.*, 1992; Médard *et al.*, 2008] with a calculated log fO₂ of -16 at our *P-T* conditions [Jakobsson and Oskarsson, 1994; Ulmer and Luth, 1991]. Experimental results from Médard *et al.* indicate that the fO₂ within graphite capsules is likely more reducing than the CCO buffer (average value: CCO-0.07; IW+1.5), therefore the amount of Fe³⁺ introduced during this process is assumed to be negligible. The sample underwent synchronized slow decompression (1 MPa/minute) and cooling (1 K/minute) to reduce cracking during recovery, but usually the cylinder of fayalite naturally separated into rough 2–3 mm-thick disks. The hot-pressing increased the bulk density and sintered the aggregate into a machinable form; the sample disks were cored to 8 mm outer diameter. The composition was checked for carbon contamination from the graphite hot-pressing sleeve on a scanning electron microscope using energy-dispersive x-ray spectroscopy, but none was found. There were minor amounts of molybdenum contamination in the form of Fe-Mo metal oxides, but total bulk Mo content was constrained to less than 2 wt% with electron microprobe analyses. The disks were then lapped down to under-fill the volume of the molybdenum sample holder (see below) by 7-13%, such that — accounting for thermal expansion of the Mo holder [Miller *et al.*, 1988] and the Fe₂SiO₄ liquid density at ambient pressure and 1300°C — a void space 1–1.5 mm-deep would remain at the top of the heated capsule. This small void space volume prevents blow out, excessive warping, or failure of the welded cap and yet remains far enough above the imaged area of the shock wave to preserve one-dimensional wave propagation.

The molybdenum sample holders are comprised of a driver plate, sample well, and cap. The outer and inner portions of the rear-surface of the driver plate and both sides of the cap were

polished to a mirror-finish with 1-micron alumina grit. For the two completed preheated shots, both caps had a thickness of 1mm, and all sample wells were 8mm in diameter and approximately 2.5mm deep. Shot 409 had a driver plate 1mm thick, and shot 396 had a 2 mm-thick driver plate. After polishing, a line profile of the driver plate topography inside the sample well was measured with a depth gauge micrometer using a 0.7 mm flat-end tip in 0.2 mm increments along the centerline, which is aligned to the streak camera slit position.

An outside contractor (Electron Beam Engineering Inc., Anaheim, CA) electron-beam welded the caps to the sample holder wells enclosing the sample to prevent leaking during experimental heating. After bake-out at 100 ± 3 °C, an initial circular pass of a defocused, low-power beam under 10^{-4} torr vacuum helps residual gases to escape; trapped volatiles could lead to bowing of the sample cap during experimental heating. Sample holders are leak-checked at room temperature in a helium bomb and additionally in a heat test chamber at 1573 K by visual inspection for escaping fayalite liquid. We note that fayalite is an especially troublesome liquid to weld into capsules due to its low melting point, high surface tension, and poor glass-forming; ten capsules were lost to bad welds in obtaining the two successful capsules that were used for our experiments.

The final driver and top hat shape were measured with a depth gauge micrometer on a digital mill table in 0.1 mm increments along the bright vertical line in Figure 2a. The sample capsules were carbon coated on both sides to ~80-200 nm thickness using a Cressington model 208C coater except for a thin rectangular masked area where the streak camera slit images the shock arrival. The layer of carbon provides an oxygen sink to reduce oxidation the molybdenum during heating, which can degrade the reflection into the streak camera [*Asimow and Ahrens, 2010*].

Preparation of room temperature (300 K) shots

One solid room-temperature (300 K) shot was performed, extending the pressure range of previous room-temperature shocks on fayalite [Chen *et al.*, 2002] from 212 GPa to 229 GPa.

This was done to verify that the highest-pressure 300 K shots (107, 161, 126, 412; See Table 2) melted during impact, which is necessary for calculation of the liquid Grüneisen parameter (γ).

Details of this calculation are in the Results section under *Grüneisen parameter*.

The sample used was a single crystal of fayalite synthesized by H. Takei [Takei, 1978]. The boule was cut perpendicular to the growth axis into an elliptical disk with a minimum diameter of 7.8 mm and a maximum diameter of 8.8 mm. The disk was doubly polished to 2 mm thickness (within ± 0.002 mm of uniform thickness). The crystal contained some glassy inclusions, but their estimated volume from electron backscatter images was less than 4%. The sample was directly mounted on a 0.5 mm tantalum driver plate and was not encapsulated. A series of fused quartz mirrors were glued to the down-range side of the driver plate and sample [cf. Mosenfelder *et al.*, 2007] for recording of the shock arrival.

Experimental setup

The experimental methods used in our study for molten materials were originally developed by Rigden *et al.* [1984] and refined by Rigden *et al.* [1988; 1989], Miller *et al.* [1988; 1991a], Chen *et al.* [1998; 2002] and Asimow *et al.* (2008). The experimental configuration is summarized here; for additional description, see Asimow and Ahrens [2010].

The experiments for this study were performed in a 90/25- mm two-stage light-gas gun; previous shots from Chen *et al.* (2002) were performed using a 40- mm propellant gun. Shots 396 and 409 were preheated with a H₂O-cooled copper induction coil powered by a 10 kW Lepel radio frequency generator [Chen and Ahrens, 1998] to 1300°C (1573 K), 95°C above the melting

point of pure Fe_2SiO_4 . For preheated experiments, the sample holders are mounted through a hole drilled in a Zircar™ alumina board and are held in place by a “guy-wire” set up in which W-Re alloy wire is threaded through two Mo posts screwed into the sample side of the target.

Tantalum flyer plates were pressed into Lexan projectiles and launched at velocities (u_{fp}) of 4.997-7.085 km/s, measured by a double-flash x-ray system and a two-magnet induction detector [Asimow *et al.*, 2008]. For all three shots reported here, the two measurements agreed to within the stated uncertainty, and the average of the two measurements was used for the u_{fp} . For room-temperature experiments (shot 412), the streak camera is electrically triggered by signals from shorting pins. For preheated shots, the camera and xenon spark lamp (which illuminates the target) are triggered using a “non-contact” system from the flyer-magnet signals and an up-down counter [Asimow and Ahrens, 2010]. The light is filmed by a Hadland Imacon 790 streak camera equipped with a 25 μm slit focused horizontally across the center of the sample holder (Figure 2a). As the shock wave reaches the free surface of the driver and later the sample cover, it changes the reflectance of the polished surface, creating a visible cutoff on the film. The shock wave velocity (U_s) through the sample is calculated from the time difference of these two cutoffs, corrected for the known shape of the driver face and cap and thermal expansion of the assembly, and subtracting the shock transit time through the Mo cap. The final shock state is calculated iteratively using the technique developed in Ridgen *et al.* [1988], which takes into account the thickness and EOS of the hot molybdenum cap. The camera writing rate was calibrated using a test streak modulated by a radio-frequency tuner at 147.9993 MHz, which provides a time signal every 6.757 ns. The streak photo was scanned at 2400 dpi in 8-bit gray scale and matched to the calibration streak scanned at the same resolution to assign each column of pixels a time value. Driver and sample cutoffs were picked by selecting the inflection point of

an arctangent function fit by cross-correlation to the gray scale values of each row of pixels parallel to the time axis (Figure 2c, shows only 3 pixel rows). If the correlation coefficient for the arctangent fit for a given pixel line was less than 0.95, then that pick was discarded. Discarding of pixels usually occurred in dark portions of the photo that were either poorly exposed or dark in the pre-experiment static photo due to imperfections in the polish. A few hundred points on either side usually constrain the driver cutoff (except in shot 396, see below); these picks are co-registered with the previously measured driver topography profiles and corrected for deviations from flat. Although tilt and bowing of the impactor and hence the shock front are often approximated as parabolic [*Mitchell and Nellis*, 1981a], we found that fourth order polynomial fits were suitable for extrapolating the shape of the shock front within the sample (Figure 2b). Only the center 3mm portion of the sample arrival was used for the calculation of shock transit time to reduce edge effects. The iterative solutions [*Rigden et al.*, 1988] to particle velocity (u_p), pressure (P_H), and density (ρ_H) of the shock state were determined from impedance matching, the Rankine-Hugoniot equations, and the following input parameters: sample geometry; standard Hugoniot data (ρ_o , C_o , s) for the metal flyer, driver and cover plates [*Asimow et al.*, 2008; *Mitchell and Nellis*, 1981b]; and the initial density (ρ_o) and best-initial guess values for 1 bar bulk sound speed (C_o) and Hugoniot slope s for fayalite liquid at 1300 °C. It should be noted that regardless of the initial guess for the C_o and s the same resulting shock state converges after three iterations). Uncertainties in all derived parameters (U_s , u_p , P_H , ρ_H) were obtained from the uncertainties in the measured and standard parameters by analytical error propagation [cf. *Jackson and Ahrens*, 1979].

RESULTS

Density and ultrasonic results at ambient pressure

The double-bob density measurements between 1551 and 1831 K are reported in Table 1 and plotted against temperature in Figure 3. A linear equation: $\rho(T) = 3699 \pm 1 - 0.30 \pm 0.01 * (T - 1573 \text{ K})$ was fit to the data. Sound speed (C) data on the same sample between 1516 and 1879 K are reported in *Ai and Lange* [2004] using a frequency-sweep acoustic interferometer. Those data can also be described as a linear function of temperature: $C(T) = 2438 \pm 5 - 0.33 \pm 0.03 * (T - 1573 \text{ K})$ m/s.

Sink/ float results

The results from the sink/float experiments are shown in Figure 4. We observed floating of the almandine garnets at 3.5 and 4.5 GPa and floating of spessartine garnets at 4.0 GPa. We were unsuccessful in observing sinks or floats at 3.0 GPa because of marker sphere dissolution or breakdown during the run. Therefore, our new data do not bracket the fayalite liquid density. However the observed floats do give a minimum density of the liquid within the experimental pressure range 3.5-4.5 GPa, and thus the new data do not agree with the sink/float measurements of *Agee* [1992] requiring that the compression curve for fayalite liquid be at higher density values in the range 3.5-4.5 GPa. On the other hand, the measurements of *Agee* [1992] at lower pressure using ruby spheres are still consistent with the new multi-anvil measurements. Reasons for possible inconsistencies in the *Agee* [1992] are discussed below.

Shockwave results

Comparison to previous data

The shock wave data are reported in Table 2, including shot number, flyer/driver material, temperature prior to firing, u_{fp} , u_p , U_s , P_H , and peak density (ρ_H). Figure 5 shows the Hugoniot of this data in U_s - u_p space. A Hugoniot is a family of shock states achieved in a

material from the same starting conditions (in this case, liquid fayalite at 1573 K and 1 bar).

Empirically the Hugoniot of a well-behaved material forms a line in U_s - u_p space, given to third order in strain by $U_s = C_o + s u_p$ [Jeanloz, 1989] where the intercept $C_o = (K_{oS} / \rho_o)^{1/2}$ is the bulk sound speed of fayalite liquid at room pressure and the slope $s = (K'_s + 1)/4$ is related to K'_s , the isentropic pressure derivative of the isentropic bulk modulus (K_{oS}) [Ruoff, 1967].

Previous work from *Chen et al.* [2002] consists of 7 experiments completed on the Caltech 40-mm propellant gun. All *Chen et al.* data are taken from the original publication and were not re-analyzed. These data have widely varying reported uncertainties; *Chen et al.*'s linear regression was weighted by errors on U_s only: $U_s = 2.63 \pm 0.02 + 1.59 \pm 0.01 u_p$ km/s.

To these data, we added two preheated shocks, extending the Hugoniot to 161 GPa. Shot 409 from this study had clear cutoffs and well-defined shock arrivals. Conversely, shot 396 had a poorly exposed driver arrival, but showed a simple, un-tilted planar shock arrival at the top hat. The driver arrival for this shot was approximated as linear and un-tilted, which introduced error in the travel time measurement but is a suitable assumption due to the flatness of the top hat. An un-weighted linear fit to all nine preheated fayalite liquid data points from *Chen et al.* [2002] and this study yields $U_s = 2.67 \pm 0.08 + 1.50 \pm 0.03 u_p$ km/s ($r^2 = 0.996$), whereas a York regression (a regression which accounts for errors in both U_s and u_p) gives $U_s = 2.80 \pm 0.18 + 1.488 \pm 0.071 u_p$ km/s (MSWD = 8.9).

The unconstrained intercept of the York fit to the full data set is consistent within the 99% confidence interval with the bulk sound speed determined to much higher precision by ultrasonic techniques, $C_o = 2.438 \pm 0.005$ km/s [Ai and Lange, 2004]. This suggests we cannot confidently reject the null hypothesis that this material, like other silicate liquids measured in the same way, displays relaxed (liquid-like), as opposed to un-relaxed (glass-like), behavior upon

shock compression [Rigden *et al.*, 1988]. Therefore, to reduce the error on the linear fit, we fixed the intercept at the ultrasonic value measured in this work. The un-weighted, constrained linear fit in U_S-u_p space yields $U_S = 2.438 \pm 0.005 + 1.58 \pm 0.03 u_p$ km/s ($r^2=0.998$). A weighted, constrained fit yields poor results because the uncertainties of U_S reported for some of *Chen et al.*'s data are anomalously small. The selected slope s corresponds to a K'_S value of 5.33 ± 0.10 , and overall this is in reasonable agreement with the previous work by *Chen et al.* [2002], which estimated K'_S of 5.39 ± 0.04 . Figure 5 includes both the unconstrained and constrained linear fits to the entire data set, as well as the previous fit by *Chen et al.* [2002]. It is worth noting that the slopes of the new and old linear fits are very similar despite having slightly different though nominally fayalitic compositions. Thus within the errors of the experiments, our results seem to be insensitive to minor compositional differences.

Our newest shockwave and sink/float results also resolve previously discrepant measurements for K'_S . Isothermal static compression data from sink/float [Agee, 1992] and shock wave [Chen *et al.*, 2002] experiments gave K' values of 10.1 and 5.36, respectively. The newest sink/float measurements are shown in Figure 4 alongside two 3rd-order Birch-Murnaghan isotherms (dashed and dotted lines). The isotherms are fit with ρ_0 from this study, the bulk modulus from ultrasonic experiments ($K_T=19.4$) [Ai and Lange, 2004], and K' from the slope of the newest constrained linear Hugoniot ($K'=5.33$)(dashed in Fig. 4) or K' from the 3rd-order Birch-Murnaghan/Mie-Grüneisen (3BM/MG) ($K'=7.28$) from this study (dotted in Fig. 4). The details of the 3BM/MG fit are given below in the *Thermal equation of state fitting* section. The solid line is calculated using the previous data from Agee [1992]. The three experiments showing flotation are consistent with the dashed and dotted lines and discount the previous measurements (>3 GPa) on identical material used in the 1992 study. It is conceivable that piston “bottoming-

out” or other unknown friction effects at high compressions and high temperatures produced lower pressures than expected from calibration runs. In any case, the new multi-anvil sink/float data are in good agreement with the ultrasonic and shockwave results.

Solid Hugoniot shocked to liquid / χ^2 test of weighted values

Shot 412 was carried out on single crystal fayalite and is believed to have undergone a phase transition to liquid during the shock. A phase transition to liquid along the Hugoniot can often be detected by an offset in pressure-volume [Akins *et al.*, 2004] or U_S - u_p space. To establish where in U_S - u_p space the phase transition occurs, we used a χ^2 test of weighted values on linear fits to all room-temperature shock data (Table 1). The goal was to minimize the χ^2 value of fitting two separate linear Hugoniot to solid and shock-melted data. Excluding shot 116, which has an anomalously low U_s , the best fit ($\chi^2 = 0.0014867$) occurred when shots 107, 161, 126, and 412 were calculated as liquids. The pressure limit of 190 GPa for shock melting implied by placing the boundary between shots 99 and 107 is also consistent with the melting thresholds along the Hugoniot of many iron-free silicate minerals shocked from room temperature: quartz at 120 GPa [J. A. Akins, 2002; Lyzenga, 1983], diopside at ≤ 144 GPa [Svendsen and Ahrens, 1990], and diopside-anorthite ($\text{Di}_{64}\text{An}_{36}$) at 133 GPa [Asimow and Ahrens, 2010] all of which have higher ambient melting temperature than that of fayalite (previous descriptions of shock melting of forsterite at 142 GPa [Mosenfelder *et al.*, 2007] enstatite at 174 GPa [Mosenfelder *et al.*, 2009] may not be accurate and are discussed in Chapter III). We have therefore used the four highest-pressure data points, presumed to have melted on shock, to calculate a value for the liquid Grüneisen parameter.

Grüneisen parameter

The thermodynamic Grüneisen parameter (γ) is a macroscopic parameter that relates

thermal pressure to the thermal energy per unit volume, where thermal pressure is defined as the increase in pressure due to heating at a constant volume. Because a solid shocked to a liquid and an initially molten sample obtain different pressures and internal energy states at equal density (ρ_H) upon compression, γ can be directly determined by comparison of the two Hugoniot (e.g., [Luo *et al.*, 2002; Mosenfelder *et al.*, 2007, Asimow & Ahrens, 2010]). We calculated the Grüneisen parameter from the following expressions; the parameter definitions and the values used are given in Table 3. By definition,

$$\gamma = \frac{1}{\rho} \left(\frac{\partial P}{\partial E} \right)_{\rho} . \quad (2)$$

The Mie-Grüneisen approximation defines γ as a function of ρ only, which simplifies the above expression to a finite difference:

$$\gamma = \frac{1}{\rho} \frac{\Delta P_{th}}{\Delta E} = \frac{1}{\rho} \frac{(P_{H-liquid} - P_{H-solid})}{\Delta E} , \quad (3)$$

where ρ is the density of interest and ΔP_{th} and ΔE are the offsets in pressure and internal energy between the two Hugoniot states at that density. The subscripts *H-liquid* and *H-solid* correspond to states on the Hugoniot that are both liquid in the shock state but that were initially a liquid at 1573 K and a solid at 300 K, respectively. The energy offset is calculated from

$$\Delta E = \Delta E_{H-solid} - \Delta E_{H-liquid} + \Delta E_{tr} , \quad (4)$$

where ΔE_{tr} , the transition energy, is the internal energy difference at ambient pressure conditions and is estimated by the enthalpy difference (ΔH_{tr}) because the transition takes place at nearly zero pressure [Asimow and Ahrens, 2010]. ΔH_{tr} is composed of two parts, the integral

of the isobaric heat capacity (C_P) and the enthalpy of fusion, and was calculated with MELTS [Ghiorso and Sack, 1995]. The internal energy change across each shock front (ΔE_H) was calculated using the 3rd Rankine-Hugoniot relation,

$$\Delta E_H = \frac{P_H}{2} \left(\frac{1}{\rho_o} - \frac{1}{\rho_H} \right) . \quad (5)$$

There are several empirical forms for describing the density dependence of $\gamma(\rho)$ consistent with the Mie-Grüneisen assumption [Stixrude and Lithgow-Bertelloni, 2005]. We will look only at the power law form, which is both the simplest and most prevalent in the literature:

$$\gamma(\rho) = \gamma_o (\rho_o / \rho)^q . \quad (6)$$

The Grüneisen parameter at initial conditions is derived from the expressions

$$\gamma = \frac{\alpha K_T}{\rho C_V} \quad (7)$$

and

$$\frac{C_P}{C_V} = 1 + \alpha \gamma T , \quad (8)$$

where α is the isobaric coefficient of thermal expansion, C_V is isochoric heat capacity, and C_P is isobaric heat capacity.

Fitting the offset between the Hugoniot of fayalite liquid shocked from liquid and solid initial states to equation (5) yields a q value of -1.45 based on data in the vicinity of $\rho_o/\rho = 0.49$. In solid materials γ generally decreases upon compression (Figure 6), but a negative q value demonstrates that γ for this liquid increases upon compression. Moreover, this q value is similar

to values obtained on other silicate liquid compositions using Hugoniot offsets, such as forsterite ($q = -1.47$) (corrected from the *Mosenfelder et al.* value, see Table 5; Chapter III includes a new EOS from preheated forsterite), enstatite ($q = -1.71$) [*Mosenfelder et al.*, 2009] (revised in Chapter III), and anorthite-diopside eutectic ($q = -1.63$) [*Asimow and Ahrens*, 2010]. We take this result as strong evidence that iron-bearing silicate liquids follow the same general behavior as iron-free silicate liquids, which are all described by $-2.0 \leq q \leq -1.45$ for the compression range $1 \geq \rho_o/\rho \geq 0.49$. Figure 6 shows the similarities in volume dependence of γ for liquids of composition MgSiO_3 (En), Mg_2SiO_4 (Fo), and Fe_2SiO_4 (Fa) as well as the opposite dependence displayed by mantle solids.

Negative q values for liquids have been interpreted qualitatively as a result of increasing cation coordination by analogy to structural phase changes in related solids [*Stixrude and Karki*, 2005] and, more recently, quantitatively in terms of liquid configurational entropy in the context of a hard-sphere model of atomic packing in liquids [*Jing and Karato*, 2011a]. The consistent behavior of fayalite with other liquids so far studied does not obviously resolve the question of the microscopic origin of the behavior, but it shows that the behavior does not depend very much on the major cations in the liquid.

Thermal equation of state fitting

A Hugoniot is a one-parameter curve through a P - V - E thermodynamic space of two independent variables, in this case $V(P, E)$. However, we are generally interested in defining the behavior of liquids in regions that lie off the Hugoniot curve. In particular, at high compressions, the Hugoniot reaches temperatures and energies much higher than mantle conditions of geophysical interest, even for the early earth. In order to investigate material properties that lie off the Hugoniot, we attempt to define the entire P - V - E surface for a given composition by fitting

a thermal equation of state. There are several formalisms for thermal EOS; we have chosen to investigate three of them (all of which are plotted in Figure 7): (1) the shock wave equation of state (SWEOS, derived from both the constrained and unconstrained linear fit above), (2) 3rd and 4th order Birch-Murnaghan Mie-Grüneisen equation of state (3BM/MG and 4BM/MG), and (3) de Koker-Stixrude fundamental relation (dKSFR) [*de Koker and Stixrude, 2009*].

The SWEOS is defined by a linear Hugoniot in $U_S - u_p$ space, transformed into pressure (P)- density (ρ) space using the first and second Rankine-Hugoniot equations [e.g., *Ahrens, 1987*]:

$$\rho_H = \frac{\rho_o U_S}{U_S - u_p} \quad (9)$$

$$P_H = \rho_o U_S u_p. \quad (10)$$

States that lie off the Hugoniot are found using the Mie-Grüneisen thermal pressure approximation with temperature-independent $\gamma(\rho)$, as calculated above (6).

The 3rd and 4th-order Birch-Murnaghan/Mie-Grüneisen equations of state are defined by 3rd or 4th order Birch-Murnaghan isentropes centered at 1 bar and 1573K plus a Mie-Grüneisen thermal pressure approximation. Thus, total pressure P at any volume and internal energy is given by

$$P = P_s + P_{th}. \quad (11)$$

P_s is the Birch-Murnaghan isentropic pressure given to 4th order in strain by

$$P_s = 3K_{os} f (1 + 2f)^{\frac{5}{2}} \left(1 + \frac{3}{2} (K'_s - 4) f + \frac{3}{2} (K''_s K_{os} + K'_s (K'_s - 7) + \frac{143}{9}) f^2 \right) \quad (12)$$

where f is the Eulerian finite strain parameter

$$f = \frac{1}{2} \left(\left(\frac{\rho}{\rho_o} \right)^{\frac{2}{3}} - 1 \right). \quad (13)$$

[Birch, 1947]. The thermal pressure term (P_{th}) is given by

$$P_{th} = \gamma \rho (E - E_S) \quad (14)$$

where E is the energy of interest. The internal energy along the isentrope (E_S) is found by integration of $dE_S = -P_S dV$:

$$E_S = \frac{9}{2} \frac{K_{os}}{\rho_o} (f^2 + (K'_S - 4)f^3 + \frac{3}{4} (K''_S K_{os} + K'_S (K'_S - 7) + \frac{143}{9}) f^4) \quad (15)$$

For 3rd-order BM isentropic pressure and energy, K'' in the previous expressions is fixed to the value that makes the 4th-order term vanish:

$$K''_S = -(K'_S (K'_S - 7) + \frac{143}{9}) / K_{os} \quad (16)$$

In order to infer a temperature, we need to define an isochoric heat capacity (C_V). Currently no shock temperature measurements exist to constrain an expression for $C_V(\rho)$ for an iron-bearing silicate liquid, so C_V was fixed at the constant value determined from constant C_P at ambient pressure and 1573 K [Lange and Navrotsky, 1992]. The temperature of interest is then calculated with the equation

$$T = T_o \int_{\rho_o}^{\rho} \frac{\gamma(\rho)}{\rho} d\rho + \int_{E_S}^E \frac{1}{C_V} dE, \quad (17)$$

which is composed of two parts: (1) integration along the reference isentrope to the density of interest with $T_0 = 1573$ K as the foot temperature and (2) addition of the energy offset proportional to C_V .

A method for fitting shock wave data to the 3BM/MG and 4BM/MG forms is found in *Asimow and Ahrens* [2010]. To account for uncertainties in both pressure and volume, the function

$$\chi^2 = \sum_{i=1}^n \left[\left(\frac{P_*^i(\rho_*^i) - P_H^i}{\sigma_\rho^i} \right)^2 + \left(\frac{\rho_*^i - \rho_H^i}{\sigma_\rho^i} \right)^2 \right] \quad (18)$$

is minimized, where pressure is evaluated along the model Hugoniot at the trial density

$$P_*^i = \frac{P_S - \gamma \rho_*^i (E_S - E_{tr}^i)}{1 - \frac{\gamma}{2} \left(\frac{\rho_*^i}{\rho_o^i} - 1 \right)}. \quad (19)$$

The subscript * denotes a trial pressure or density, and σ denotes the respective uncertainties for each pressure-density experimental pair, (P_H^i, ρ_H^i) . Uncertainties in the fitted parameters are estimated by bootstrap iteration [Efron, 1982]. The input parameters that remain fixed are K_{oS} , C_V , ρ_o , and γ_o ; the best-fit parameters (K'_S and q , plus K'' for 4BM) are given in Table 4. The 3BM/MG fit result is $K'_S = 7.28 \pm 0.35$, $q = -0.95 \pm 0.51$, and a reduced $\chi^2 = 1.526$. The 4BM/MG fit result is $K'_S = 6.64 \pm 0.58$, $K'' = -0.47 \pm 0.27 \text{ GPa}^{-1}$, $q = -0.54 \pm 1.49$ and reduced $\chi^2 = 0.941$. The 4BM/MG chi-squared value indicates probable over-fitting, and the fairly large error bars on all output parameters seem to indicate a very unstable fitting routine. On the other hand, the 3BM/MG seems relatively stable. The unconstrained-SWEOS appears to have similar form to the 3BM/MG and matches the highest pressure data better than the constrained SWEOS. The

stiffness in the constrained SWEOS is likely due to being tied to the intercept and the most precise of *Chen et al.*'s data points—the precision of which is likely overestimated. The q value for the SWEOS is just within the stated errors of the 3BM/MG value, and the 3BM/MG reduced chi-squared value is reasonable. Additionally with little justification to implement the 4th-order fit, we recommend the 3rd-order fit for fayalite liquid.

The initially solid data are included in the fits to the 3BM/MG and 4BM/MG thermal EOS for the liquid (figure 7). The 4th-order fit recovers these data very well, but only the 3rd-order fit appears justified by the fitting statistics.

The Eulerian finite strain Birch-Murnaghan EOS has been used widely in the literature for describing the volumetric behavior of liquids [*Agee, 1998; Y Ai and Lange, 2008; Asimow and Ahrens, 2010; Bottinga, 1985; Lange, 2007; Rigden et al., 1989; Suzuki et al., 1995; Tenner et al., 2007*]; it has thus far proven to be adequate for fitting although it lacks any rigorous basis in theory as an EOS for liquids. The BM formalism has been criticized for its theoretical weakness in giving unphysical interatomic potentials for high K' materials (gases and liquids) [*Hofmeister, 1993*] and for singularities that occur at high temperature and low pressure [*Ghiorso, 2004*]. Consequently, although the BM EOS can fit our data and allows interpolation between experimental points, it should be used only with caution for extrapolation beyond experimental constraints.

It is a difficult task to capture the nature of liquids, which have short-range order but lack long-range order, in a single EOS. Two recent EOS formalisms have been developed specifically for silicate liquids that are both thermodynamically and theoretically self-consistent in their approach to describing the volume behavior at elevated temperatures and pressure: (1) the deKoker and Stixrude fundamental relation (dKSFR) [*de Koker and Stixrude, 2009*] and (2) the

hard sphere equation of state (HSEOS) [*Jing and Karato, 2011a*].

The dKSFR is an extension of the finite strain description given in *Birch* [1952; 1978] but additionally takes into account the thermal free energy contribution and temperature dependence of liquid properties. The thermodynamic variables are self-consistent in that they are derived from a single equation for the Helmholtz energy, and the contributions to the Helmholtz energy are separable [*McQuarrie, 1984*] into an ideal gas term, an excess term, and an electronic term. Recent work by *Muñoz Ramo and Stixrude* [in review] using first principles molecular dynamics (FPMD, GGA+U) of Fe_2SiO_4 liquid obtained a fit with a fourth-order expansion in finite strain and first-order expansion in the reduced temperature using the dKSFR. Their Hugoniot, shown in Figure 7, is in good agreement with our shockwave data. However, contrary to the monotonic increase in γ with increasing pressure inferred from shock wave studies, their results show γ increasing up to a compression of $\rho_o/\rho \approx 0.49$ followed by a decrease in γ coinciding with a change from the high-spin state of Fe.

The HSEOS assigns a hard sphere for each cation species, which move freely in the liquid. The geometrical arrangement of these spheres gives the contribution of entropy to the compression of the liquid [*Jing and Karato, 2011a*]. This formalism does well in explaining the complex behaviors of melts, such as the dependence of γ with pressure. However currently, the calibration of the Fe sphere diameter is based on two experiments within a close range of temperature. Therefore, the Fe sphere diameter dependence on temperature remains somewhat poorly constrained for extreme temperature conditions along the Hugoniot. Calibration would be improved with shock temperature measurements or any other independent measurements of Fe-bearing silicate liquids within a wider temperature range.

Corrections and re-analysis of silicate liquids

Also in this study, the anorthite and diopside liquid data of *Asimow and Ahrens* [2010] were re-analyzed, only sampling the center 3 mm of the arrival top hat. This was motivated by a hydro-code model of shock propagation through our capsule geometry carried out at Lawrence Livermore National Laboratory by J. Nguyen, which indicated that the outer part of the top hat arrival is influenced by edge effects. The corrected BM/MG fits are given in Table 5, and the reanalyzed data points are given in Table 1 of Chapter III. The 4th-order fit for anorthite liquid excludes 3 shots: 382, the highest pressure shot from *Asimow and Ahrens* [2010], due to an abnormally shaped shock arrival; and shots 663 and 672, the highest pressure shots from Rigden [1988] due to possible un-relaxed behavior upon compression. For further discussion of glass-like behavior in anorthite under some shock conditions, see *Asimow and Ahrens* [2010], section 4.4. The re-analysis of diopside liquid excludes 378, the lowest pressure shot from *Asimow and Ahrens* [2010] due to irregular and over-exposed top hat arrival.

Also presented in Table 5 is the corrected forsterite liquid γ_0 (which previously contained a sign error), and its subsequent re-fitted 4BM parameters. The entire EOS of forsterite is revised in Chapter III.

IMPLICATIONS

Mixing of oxide volumes at high pressure and temperature; application to a magma ocean liquidus

Our extension of the EOS of fayalite liquid completes the basis set needed for estimation, subject to the assumption of linear mixing, of liquid densities in the full CMASF (CaO-MgO-Al₂O₃-SiO₂-FeO) major element space for mafic to ultramafic liquids at elevated temperatures and pressures. Shockwave experiments completed thus far that span this component space are

forsterite (Fo, Mg_2SiO_4) [Mosenfelder *et al.*, 2007], enstatite (En, MgSiO_3) [Mosenfelder *et al.*, 2009], anorthite (An, $\text{CaAl}_2\text{Si}_2\text{O}_8$), diopside (Di, $\text{CaMgSi}_2\text{O}_6$) [Asimow and Ahrens, 2010], and now also fayalite (Fa, Fe_2SiO_4). All of the EOS parameters for each of these compositions, corrected (see above) or recommended by the original authors, are given in Table 5. The revised EOS are discussed in detail in the subsequent chapter (Tables 3 and 4)

In this study we examine only one simple model of many possible scenarios for the crystallization of an early terrestrial magma ocean. Our initial condition is a well-mixed, convecting liquid composed of one of two plausible bulk silicate Earth compositions — “chondrite” or peridotite — that reaches the base of the mantle. To learn at what depth and critical potential temperature such a whole-mantle magma ocean would begin to crystallize, we used mixtures of silicate liquids in the CMASF system and calculated the intersections or tangency points between isentropes of these two liquid compositions and their respective liquidus curves. The basis of our model is derived from an alternative definition of the Grüneisen parameter,

$$\gamma = (\partial \ln T) / (\partial \ln \rho)_s, \quad (20)$$

which expresses the adiabatic temperature gradient with increasing density [Miller *et al.*, 1991b]. Figure 8 shows the two mantle compositions that we examined. The first (Fig. 8a) is a synthetic “chondrite” mix [Andrault *et al.*, 2011] with relative proportions of the five major oxides akin to the primitive mantle but lacking any minor components (TiO_2 , Na_2O , K_2O ... etc.); its major element ratios are similar to pyrolite composition [Ringwood, 1975]. The second composition (Fig. 8b) approximates the major oxide composition of KLB-1 peridotite [Fiquet *et al.*, 2010], a fertile spinel lherzolite. We also considered the KLB-1 composition given by Davis *et al.* [2009], but found that the isentropes were nearly indistinguishable from those calculated from the

published composition in *Fiquet et al.* [2010]. Table 6 gives the major oxide proportions for each composition as well as the normalized percent of each end-member liquid used in the model. We also were concerned with what the density contrast of our model liquid would be with its first forming solid—whether it would sink or float. As a conservative measure of where solid flotation is possible, we assumed the liquidus solid to be pure Pv (MgSiO_3 , magnesium perovskite) using the EOS from *Mosenfelder et al.* [2009]. Mg-rich Pv was the liquidus solid in both *Andrault et al.* [2011] and *Fiquet et al.* [2010] at the pressures of interest.

We determined each CMASF model isentrope for a given potential temperature (T_P) in a stepwise fashion, solving for temperature (T) at each fixed increment of pressure (P) from 0 to 140 GPa. In this calculation, each CMASF isentrope is a combination of the pure end-member isentropes of An, Di, Fo, En, and Fa; and each of the end-member isentropes is defined by its own potential temperature T_P^i (superscript i denotes an end-member mineral), where T_P^i is a separately defined value from the T_P of the CMASF model isentrope. The separate T_P and T_P^i values permit the mixture of the end-member isentropes to define a point on the final CMASF model isentrope in which the total entropy (S_{tot}) remains a constant, such that

$$S_{tot} = \sum_i f^i S^i + S_{mix} = \text{constant}, \quad (21)$$

where f is the mole fraction (Table 6) and S^i is the molar entropy for each end-member in the model liquid. By assuming the entropy of mixing (S_{mix}) is constant for a given liquid composition, the potential temperature of each end-member liquid isentrope (T_P^i) was solved by setting the derivative of the total entropy equal to zero:

$$d \sum_i f^i S^i = \sum_i f^i C_P^i \ln \left(\frac{T_P^i}{T_P} \right) = 0. \quad (22)$$

The potential temperature for each end-member liquid isentrope is further defined as

$$T_p^i = T \exp \left(\frac{\gamma_o^i \left(\frac{V_p^i}{V_o^i} \right)^{q^i}}{q^i} - \left(\frac{V^i}{V_o^i} \right)^{q^i} \right). \quad (23)$$

This expression is derived from (20) by integrating

$$\partial T = \gamma_o \left(\frac{\rho_o}{\rho} \right)^q \frac{T}{\rho} \partial \rho. \quad (24)$$

and is dependent on the following three variables: (1) the temperature at each iteration along the model isentrope (T), (2) the volume of each end member at T and P (V^i), and (3) the volume of each end member at T_p^i and 0 GPa (V_p^i). These three variables are solved iteratively to satisfy equation (22) and to minimize the expression

$$\sum_i (P_s^i - P) + (P_p^i)^2, \quad (25)$$

where P_p^i is the BM isentropic pressure at T_p^i and equals 0 GPa at the target volume V_p^i and P_s^i is the BM isentropic pressure for each end member at T . Minimization of this expression ensures that the isentropic pressure for each end member converges to the defined pressure in question and that P_p^i is in fact equal to 0 GPa. For Fa, we used the BM3 parameters given in Table 4; for all other end members, we used the BM parameters in Table 5. In total, 11 parameters (T and two volumes, V^i and V_p^i , for each of the 5 end members) were solved iteratively for each step increment in pressure along a model isentrope.

The densities of the mixtures were calculated using linear mixing of volumes. This assumption has been previously tested for mixing of anorthite and diopside liquids [Asimow and Ahrens, 2010] and was found to be well-behaved at high temperatures and pressures but began to break down when applied at low temperatures requiring very large extrapolation downwards from the Hugoniot temperature. Furthermore, anorthite liquid may be a special case due to its highly polymerized structure at low pressure [Mysen and Richet, 2005], although we examine

this further in Chapter III. Hence, despite examination of three compositions along the anorthite-diopside join, it remains unclear whether or not linear mixing of volume at high pressure is valid for most mafic to ultramafic silicate liquids. Nevertheless, given five measured compositions in a five-oxide system, the assumption of linear mixing is necessary to make progress at this time and remains consistent with data presently available. We examine this assumption in detail in Chapter IV.

The resulting model for the *Andrault et al.* [2011] “chondrite” mix shows that crystallization would begin at the base of present-day mantle (~135 GPa) with a critical adiabat of $T_p = 2600\text{K}$ (Fig 8a). *Andrault et al.* found Pv to be the liquidus phase at all pressures above 60 GPa; therefore we calculated the density for a first forming crystal and found it to be denser than the surrounding liquid ($\rho_{\text{Pv}}, 5.38 \text{ g cm}^{-3} > \rho_{\text{liquid}}, 5.28 \text{ g cm}^{-3}$). Thus a basal magma ocean similar to that described in *Labrosse et al.* [2007] in which a large portion of the lowermost mantle is zone-refined to concentrate incompatible elements would be unlikely as crystallization of the mantle would occur from the bottom up. A chondritic basal magma ocean is likely only able to exist within the thermal boundary layer (highest estimated outer core of 4150K) [*Hernlund et al.*, 2005] or at the elevated basal temperatures that occurred during early Earth accretion [*Canup*, 2004].

The critical adiabat for the peridotite composition of *Fiquet et al.* (2010), on the other hand, occurs at a higher T_p of 2800 K and, notably, is tangent to the liquidus at 85 GPa (Fig 8b). Consequently crystallization would begin in the middle of the lower mantle. A Pv liquidus phase would, like the model above, sink upon formation ($\rho_{\text{Pv}}, 4.94 \text{ g cm}^{-3} > \rho_{\text{liquid}}, 4.63 \text{ g cm}^{-3}$). This model is more akin to the picture described in *Labrosse et al.* [2007] as the basal magma ocean would include a portion of the lower mantle which could be used to distill incompatible elements

into a potential present-day ULVZ, yet the sinking liquidus phase is not conducive to the dynamic formation of a basal ocean.

It is worth mentioning that the surface temperatures in both of these models could be too hot for simple, realistic magma ocean models; *Andraut et al.* [2011] suggest that such high surface temperatures would lead to large portions of the mantle vaporizing and rapid cooling if thermal blanketing is inefficient.

Within this exercise, the location of first crystallization is likely dominantly controlled by two factors: (1) the topology of the liquidus curve and (2) the amount of Fo end-member in the model liquid. It is unclear whether different shapes of liquidus curves stem from differing experimental techniques in the two synchrotron-based laser-heated diamond anvil studies considered or instead if they reflect thermodynamic differences within that range of composition space. However, Fig. 8 makes clear that without a notable decrease in slope in the liquidus curve compared to the isentrope at high pressure, crystallization would always be predicted at the base of the mantle (Fig. 8b).

Secondly, it has been observed that the forsterite component has a large control on the spacing and steepness of the isentropes. This behavior can be seen to be true in peridotite, which has a greater fraction of Fo component (Table 6) and has a much steeper isentrope series than the En-rich chondrite liquid (Fig. 8). The effect that Fo has on the isentrope mixing can be predicted from its 1-bar thermodynamic parameters (Table 5) with larger γ_o , α , and K_S . These larger parameters are inversely proportional to the amount of SiO₂ in Fo, since the dV/dT value of SiO₂ at ambient pressure (from which these parameters are derived) is zero [*Lange and Carmichael*, 1990]. The bulk modulus of SiO₂ is notably low compared to other oxides likely because of topological degrees of freedom in tetrahedral framework liquids. Thus the component with the

least SiO₂ gives the largest γ_o , α , and K_S and so the steepest isentrope, which contributes directly to the steepness of the isentrope of the mixture.

In Chapter III, we used the revised EOS of Fo, An, and En to re-model these liquid isentropes (Figure 7). The results are fairly similar, but it is important to note that the γ_o , α , and K_S of forsterite liquids are not as large as modeled by the 1-bar data, and thus forsterite does not play such a dominant role on the steepness of the isentrope. A full discussion is given in Chapter III, section *Isentropes for a full mantle magma ocean*.

We can conclude from this exercise in modeling the Earth's accretion, acknowledging the simplifying assumptions and presumed bulk compositions, that the first crystallizing solid will likely occur within the lower mantle or at the base of the mantle. This is made more likely if early earth core temperatures are assumed to be elevated above current estimates [*Canup*, 2004]. Although largely controlled by the chosen bulk composition, within our exercise the liquidus phase would be Pv and would sink upon formation. Whether pure Mg-Pv is a correct approximation to the liquidus phase, as opposed to a more Fe-rich (Mg,Fe)-Pv, is unclear based on the spread of high *T-P* Fe partitioning values in the current literature ($D_{Fe} = 0.6$ to > 0.1) [*Andrault et al.*, 2012; *Nomura et al.*, 2011]. Regardless, since pure Pv is the least dense end-member of the (Mg, Fe)SiO₃ solid-solution, greater partitioning of Fe into the solid would only further increase the density and magnitude of the already observed negative buoyancy.

Buoyancy in the current temperature regime; application to the solidus and ULVZ

For long-term gravitational stability, a presumed molten silicate liquid of the ULVZ must be denser than or at least neutrally buoyant compared to the ambient lower-most mantle bulk composition that exists today. Shown in Figure 9 are the densities of fayalite, enstatite and forsterite liquids along a plausible modern mantle adiabat including a thermal boundary

correction, with a potential temperature of 1673 K and a gradient of 10 K/GPa. A pure molten fayalite composition with density of 7 g cm^{-3} would pond at the core mantle boundary if present, as it is much denser than any likely solid assemblage at lowermost mantle conditions. However the model of a pure fayalite liquid ULVZ is inconsistent both with the density of 6.12 g cm^{-3} in the ULVZ inferred from seismic reflection coefficients [Rost *et al.*, 2006] (Figure 9) and with the non-zero shear velocity of this layer. Instead, a less-dense multicomponent partial melt needs to be considered as a plausible state for the ULVZ. Assuming linear mixing of the oxide volumes calculated from the BM EOS given in Tables 4 and 5, Figure 10a displays lines of constant density within a Fa-Fo-En-Fs space (where ferrosilite (Fs) = $\text{En} + .5\text{Fo} - .5\text{Fa}$). Figure 10b is the same plot, but uses the revised EOS in Chapter III Tables 3 and 4. The y-axis is Mg# (Mg# = $\text{MgO}/(\text{FeO} + \text{MgO})$), and the x-axis is $(\text{MgO} + \text{FeO})/\text{SiO}_2$. The solid curves delineate compositions that are neutrally buoyant with respect to a pure Pv solid at $\sim 135 \text{ GPa}$ (roughly the pressure at the CMB) at the given temperature conditions (3900 K–4500 K). The dashed lines indicate a constant density of 6.12 g cm^{-3} , which represents the estimated upper limit of a 10% density jump of an ULVZ [Rost *et al.*, 2006] with respect to PREM [Dziewonski and Anderson, 1981]. Any liquid mixture that lies above the solid lines where Pv sinks (white in Fig. 10) is inferred to be gravitationally unstable with respect to upwards percolation into the solid mantle, and any mixture below the dashed lines is denser than has been inferred for ULVZs.

In this exercise, potential liquid compositions for a high-melt fraction ULVZ must span a narrow range in composition space (striped blue in Figure 10), eliminating pure enstatite, and fayalite end-members as candidate compositions. Previously (Fig. 10a), pure forsterite was not denser than coexisting Pv crystal, but in the revised EOS (Fig. 10b), this is no longer shown to be true. For reference, the simplified chondrite and peridotite liquids modeled in the section above

are also plotted on Figure 10. These results indicate that these liquid compositions are unlikely to be gravitationally stable at the CMB today (although peridotite liquid is denser than previously modeled Fig 10b); if residual liquids were to be derived from magma oceans of either composition, they would need to be enriched in Fe, depleted in Si, or both during some process of re-crystallization and distillation from the original bulk mantle. The gray arrows from each composition indicate the direction of compositional evolution if Pv (MgSiO_3 , En) were to crystallize and be removed. It also gives a rough estimate of what the final liquid composition would need to be for Pv to be buoyant.

When evaluating whether a liquid would be gravitationally stable, Figure 10 assumes that a pure Pv end member is an acceptable estimation for bulk lower mantle density. Adding Fe to the pertinent solid phase in this scenario (modeled as Pv) would qualitatively narrow the region of gravitationally stable liquids to only low Mg# (<0.5) compositions in Fig. 10 (blue-lined area). Also the densities shown here are for fixed compositions that are unlikely to be in chemical equilibrium. For a complete examination of stability, we would need a better grasp on the actual bulk composition of the solid and an understanding of Fe/Mg partitioning at lower mantle conditions. Moreover, it is likely that the bulk lower mantle contains some amount of iron-bearing Pv and calcium-silicate Pv, which would be denser than pure Mg-Pv and also effectively narrow the range of acceptable, stable compositions for a ULVZ liquid shown in Figure 10. Similarly, incorporation of Al_2O_3 and CaO into the model partial melt using the EOS of anorthite and diopside would narrow this same region of Fig. 10 by decreasing the density of the liquid. Therefore, our simplified model in Fig. 10 indicates the minimum amount of Fe enrichment that the liquid must have to be a high-fraction, gravitationally stable silicate melt at the CMB, but the amount of enrichment is likely to be much greater.

CONCLUSIONS

The density for Fe_2SiO_4 liquid as well as values for K and K' have been constrained. Additionally, the Grüneisen parameter for Fe-bearing silicate liquids is shown to change with compression in a manner similar to non-Fe bearing liquids and the opposite to that of solids. Although the Grüneisen parameter has been measured for formulation of a thermal equation of state, as with any thermal EOS formalism, there are trade-offs especially when examining states far from the Hugoniot including extrapolations in pressure beyond experimental pressures (161 GPa). Temperature estimates could be greatly improved by either shock temperature measurements or any other off-Hugoniot temperature measurements to constrain C_v . Constraints on the end-member liquid fayalite EOS permit interpolation between CMASF silicate liquids densities, assuming linear mixing of volumes. The calculation of isentropes at elevated temperatures and pressures for model whole-mantle magma oceans composed of peridotite and simplified “chondrite” liquid indicate crystallization initiating at the mid-lower mantle (85 GPa) and the base of the mantle, respectively. Finally, a compositional range of gravitationally stable liquids was determined to examine the likelihood of a gravitationally stable ULVZ composed of a large degree of partial melt. There exists a region of melt composition that is denser than P_v at the CMB, but neither chondrite nor peridotite is sufficiently enriched in Fe to be stable. Fractional crystallization of P_v would need to take place before either liquid would be dense enough to remain at the CMB. To elucidate fully the proper stable liquid composition, formulation of multicomponent phase equilibria or partition coefficients at high pressure and temperature are necessary for accurate description of the CMB.

ACKNOWLEDGEMENTS

The authors would like to thank the following: the shock wave lab technical staff—Michael Long, Erapodito Gelle, and Russel Oliver; additionally, Bjorn Mysen for conducting Mössbauer measurements, and Jeff Nguyen for running simulations of our shock wave experiments. This work was supported by the National Science Foundation through award EAR-0855774.

REFERENCES

- Agee, C. B. (1988), Mass balance and phase density constraints on early differentiation of chondritic mantle, *Earth and planetary science letters*, 90(2), 144.
- Agee, C. B. (1992), Isothermal compression of molten Fe₂SiO₄, *Geophys. Res. Lett.*, 19(11), 1169–1172.
- Agee, C. B. (1998), Crystal-liquid density inversions in terrestrial and lunar magmas, *Physics of The Earth and Planetary Interiors*, 107(1-3), 63-74.
- Ahrens, T. J. (1987), 6. Shock Wave Techniques for Geophysics and Planetary Physics, in *Methods in Experimental Physics*, edited by G. S. Charles and L. H. Thomas, pp. 185-235, Academic Press.
- Ai, Y and R. A. Lange (2004), An ultrasonic frequency sweep interferometer for liquids at high temperature: 2. Mechanical assembly, signal processing, and application, *J. Geophys. Res.*, 109(B12204).
- Ai, Y., and R. A. Lange (2008), New acoustic velocity measurements on CaO-MgO-Al₂O₃-SiO₂ liquids: Reevaluation of the volume and compressibility of CaMgSi₂O₆-CaAl₂Si₂O₈ liquids to 25 GPa, *J. Geophys. Res.*, 113(B4), B04203.
- Akins, J. A. (2002), Dynamic compression of SiO₂: A new interpretation, *Geophysical research letters*, 29(10), 31.
- Akins, J. A., S.-N. Luo, P. D. Asimow, and T. J. Ahrens (2004), Shock-induced melting of MgSiO₃ perovskite and implications for melts in Earth's lowermost mantle, *Geophys. Res. Lett.*, 31(14), L14612.
- Andrault, D., N. Bolfan-Casanova, G. L. Nigro, M. A. Bouhifd, G. Garbarino, and M. Mezouar (2011), Solidus and liquidus profiles of chondritic mantle: Implication for melting of the Earth across its history, *Earth and planetary science letters*, 304(1-2), 251-259.
- Andrault, D., S. Petitgirard, G. Lo Nigro, J.-L. Devidal, G. Veronesi, G. Garbarino, and M. Mezouar (2012), Solid-liquid iron partitioning in Earth's deep mantle, *Nature*, 487(7407), 354-357.
- Asimow, P. D., and T. J. Ahrens (2010), Shock compression of liquid silicates to 125 GPa: The anorthite-diopside join, *J. Geophys. Res.*, 115(B10), B10209.
- Asimow, P. D., D. Sun, and T. J. Ahrens (2008), Shock compression of preheated molybdenum to 300 GPa, *Physics of The Earth and Planetary Interiors*, 174(1-4), 302.
- Birch, F. (1947), Finite Elastic Strain of Cubic Crystals, *Physical review*, 71(11), 809.
- Birch, F. (1952), Elasticity and constitution of the Earth's interior, *J. Geophys. Res.*, 57(2), 227-286.
- Birch, F. (1978), Finite strain isotherm and velocities for single-crystal and polycrystalline NaCl at high pressures and 300K, *J. Geophys. Res.*, 83(B3), 1257-1268.
- Bottinga, Y. (1985), On the isothermal compressibility of silicate liquids at high pressure, *Earth and planetary science letters*, 74(4), 350-360.
- Canup, R. M. (2004), Simulations of a late lunar-forming impact, *Icarus*, 168(2), 433-456.
- Chen, G. Q., and T. J. Ahrens (Eds.) (1998), *Radio frequency heating coils for shock wave experiments*, 63-71 pp., Materials Research Society Symposia Proceedings, Warrendale, PA.
- Chen, G. Q., T. J. Ahrens, and E. M. Stolper (2002), Shock-wave equation of state of molten and solid fayalite, *Physics of The Earth and Planetary Interiors*, 134(1-2), 35-52.
- Circone, S., and C. B. Agee (1996), Compressibility of molten high-Ti mare glass: Evidence for

- crystal-liquid density inversions in the lunar mantle, *Geochimica et Cosmochimica Acta*, 60(14), 2709-2720.
- Davis, F. A., J. A. Tangeman, T. J. Tenner, and M. M. Hirschmann (2009), The composition of KLB-1 peridotite, *American Mineralogist*, 94(1), 176-180.
- de Koker, N., and L. Stixrude (2009), Self-consistent thermodynamic description of silicate liquids, with application to shock melting of MgO periclase and MgSiO₃ perovskite, *Geophysical Journal International*, 178(1), 162 Erratum Ibid., doi: 110.1111/j.1365-1246X.2010.04739.x.
- Dziewonski, A. M., and D. L. Anderson (1981), Preliminary reference Earth model, *Physics of The Earth and Planetary Interiors*, 25(4), 297-356.
- Efron, B. (Ed.) (1982), *The Jackknife, the Bootstrap, and Other Resampling Plans*, 92 pp., Philadelphia, PA.
- Fiquet, G., A. L. Auzende, J. Siebert, A. Corgne, H. Bureau, H. Ozawa, and G. Garbarino (2010), Melting of Peridotite to 140 Gigapascals, *Science*, 329(5998), 1516-1518.
- Garnero, E. J., and D. V. Helmberger (1995), A very slow basal layer underlying large-scale low-velocity anomalies in the lower mantle beneath the Pacific: evidence from core phases, *Physics of The Earth and Planetary Interiors*, 91(1-3), 161-176.
- Ghiorso, M. S. (2004), An equation of state for silicate melts. III. Analysis of stoichiometric liquids at elevated pressure: shock compression data, molecular dynamics simulations and mineral fusion curves, *Am J Sci*, 304(8-9), 752-810.
- Ghiorso, M. S., and R. O. Sack (1995), Chemical mass transfer in magmatic processes IV. A revised and internally consistent thermodynamic model for the interpolation and extrapolation of liquid-solid equilibria in magmatic systems at elevated temperatures and pressures, *Contributions to Mineralogy and Petrology*, 119(2), 197-212.
- Hernlund, J. W., C. Thomas, and P. J. Tackley (2005), A doubling of the post-perovskite phase boundary and structure of the Earth's lowermost mantle, *Nature*, 434(7035), 882-886.
- Hofmeister, A. M. (1993), Interatomic potentials calculated from equations of state: Limitation of finite strain to moderate K', *Geophys. Res. Lett.*, 20(7), 635-638.
- Holloway, J. R., V. Pan, and G. Gudmundsson (1992), High-pressure fluid-absent melting experiments in the presence of graphite; oxygen fugacity, ferric/ferrous ratio and dissolved CO₂, *European Journal of Mineralogy*, 4(1), 105-114.
- Jackson, I., and T. J. Ahrens (1979), Shock wave compression of single-crystal forsterite, *Journal Name: J. Geophys. Res.; (United States); Journal Volume: 84:B6, Medium: X; Size: Pages: 3039-3048.*
- Jakobsson, S., and N. Oskarsson (1994), The system C-O in equilibrium with graphite at high pressure and temperature: An experimental study, *Geochimica et Cosmochimica Acta*, 58(1), 9-17.
- Janz, G. (1980), Molten Salts Data as Reference Standards for Density, Surface Tension, Viscosity, and Electrical Conductance: KNO₃ and NaCl, *Journal of Physical and Chemical Reference Data*, 9(4), 791.
- Jeanloz, R. (1989), Shock Wave Equation of State and Finite Strain Theory, *J. Geophys. Res.*, 94.
- Jing, Z., and S.-i. Karato (2011a), A new approach to the equation of state of silicate melts: An application of the theory of hard sphere mixtures, *Geochim. Cosmochim. Acta*.
- Labrosse, S., J. W. Hernlund, and N. Coltice (2007), A crystallizing dense magma ocean at the base of the Earth's mantle, *Nature*, 450(7171), 866-869.

- Lange, R. A. (2007), The density and compressibility of KAlSi_3O_8 liquid to 6.5 GPa, *American Mineralogist*, 92(1), 114-123.
- Lange, R. A., and I. S. E. Carmichael (1987), Densities of $\text{Na}_2\text{O-K}_2\text{O-MgO-MgO-FeO-Fe}_2\text{O}_3$ $\text{Al}_2\text{O}_3\text{-TiO}_2\text{-SiO}_2$ liquids: New measurements and derived partial molar properties, *Geochimica et Cosmochimica Acta*, 51(11), 2931-2946.
- Lange, R. A., and I. S. E. Carmichael (1990), Thermodynamic properties of silicate liquids with emphasis on density, thermal expansion and compressibility, *Reviews in Mineralogy and Geochemistry*, 24(1), 25-64.
- Lange, R. A., and A. Navrotsky (1992), Heat capacities of Fe_2O_3 -bearing silicate liquids, *Contributions to Mineralogy and Petrology*, 110(2-3), 311.
- Lay, T., E. J. Garnero, and Q. Williams (2004), Partial melting in a thermo-chemical boundary layer at the base of the mantle, *Physics of The Earth and Planetary Interiors*, 146(3-4), 441-467.
- Lyzenga, G. A. (1983), Shock temperatures of SiO_2 and their geophysical implications, *Journal of geophysical research*, 88(B3), 2431.
- Mao, W. L., H.-k. Mao, W. Sturhahn, J. Zhao, V. B. Prakapenka, Y. Meng, J. Shu, Y. Fei, and R. J. Hemley (2006), Iron-Rich Post-Perovskite and the Origin of Ultralow-Velocity Zones, *Science*, 312(5773), 564-565.
- McQuarrie, D. A. (1984), *Statistical Mechanics*, University Science Books, Sausalito, CA.
- Médard, E., C. A. McCammon, J. A. Barr, and T. L. Grove (2008), Oxygen fugacity, temperature reproducibility, and H_2O contents of nominally anhydrous piston-cylinder experiments using graphite capsules, *American Mineralogist*, 93(11-12), 1838-1844.
- Miller, G. H., T. J. Ahrens, and E. M. Stolper (1988), The equation of state of molybdenum at 1400 C, *Journal of Applied Physics*, 63(9), 4469-4475.
- Miller, G. H., E. M. Stolper, and T. J. Ahrens (1991a), The Equation of State of a Molten Komatiite 1 Shock Wave Compression to 36 GPa, *J. Geophys. Res.*, 96.
- Miller, G. H., E. M. Stolper, and T. J. Ahrens (1991b), The Equation of State of a Molten Komatiite 2. Application to Komatiite Petrogenesis and the Hadean Mantle, *J. Geophys. Res.*, 96.
- Mitchell, A. C., and W. J. Nellis (1981a), Diagnostic system of the Lawrence Livermore National Laboratory two-stage light-gas gun, *Review of scientific instruments*, 52(3), 347.
- Mitchell, A. C., and W. J. Nellis (1981b), Shock compression of aluminum, copper, and tantalum, *Journal of Applied Physics*, 52(5), 3363-3374.
- Mosenfelder, J. L., P. D. Asimow, and T. J. Ahrens (2007), Thermodynamic properties of Mg_2SiO_4 liquid at ultra-high pressures from shock measurements to 200 GPa on forsterite and wadsleyite, *J. Geophys. Res.*, 112.
- Mosenfelder, J. L., P. D. Asimow, D. J. Frost, D. C. Rubie, and T. J. Ahrens (2009), The MgSiO_3 system at high pressure: Thermodynamic properties of perovskite, postperovskite, and melt from global inversion of shock and static compression data, *J. Geophys. Res.*, 114.
- Muñoz Ramo, D., and L. Stixrude (in review), Spin crossover in Fe_2SiO_4 liquid at high pressure, *Physical Review Letters*.
- Mysen, B. O., and P. Richet (2005), *Silicate Glasses and Melts: Properties and Structure*, 544., Elsevier, Amsterdam.
- Nomura, R., H. Ozawa, S. Tateno, K. Hirose, J. Hernlund, S. Muto, H. Ishii, and N. Hiraoka

- (2011), Spin crossover and iron-rich silicate melt in the Earth's deep mantle, *Nature*, 473(7346), 199-202.
- Rigden, S. M., T. J. Ahrens, and E. M. Stolper (1984), Densities of liquid silicates at high pressures, *Science*, 226(4678), 1071-1074.
- Rigden, S. M., T. J. Ahrens, and E. M. Stolper (1988), Shock compression of molten silicate: results for a model basaltic composition, *J. Geophys. Res.*, 93(B1), 367-382.
- Rigden, S. M., T. J. Ahrens, and E. M. Stolper (1989), High-Pressure Equation of State of Molten Anorthite and Diopside, *Journal of Geophysical Research*, 94(B7), 9508-9522.
- Ringwood, A. E. (1975), Composition and Petrology of the Earth's Mantle, edited, p. 618, McGraw-Hill, New York.
- Rost, S., E. J. Garnero, and Q. Williams (2006), Fine-scale ultralow-velocity zone structure from high-frequency seismic array data, *J. Geophys. Res.*, 111(B9), B09310.
- Ruoff, A. (1967), Linear Shock-Velocity-Particle-Velocity Relationship, *Journal of Applied Physics*, 38(13), 4976.
- Stixrude, L., and B. Karki (2005), Structure and Freezing of MgSiO₃ Liquid in Earth's Lower Mantle, *Science*, 310(5746), 297-299.
- Stixrude, L., and C. Lithgow-Bertelloni (2005), Thermodynamics of mantle minerals – I. Physical properties, *Geophysical Journal International*, 162(2), 610-632.
- Stolper, E., D. Walker, B. H. Hager, and J. F. Hays (1981), Melt Segregation From Partially Molten Source Regions: The Importance of Melt Density and Source Region Size, *J. Geophys. Res.*, 86.
- Suzuki, A., E. Ohtani, and T. Kato (1995), Floatation of diamond in mantle melt at high pressure, *Science*, 269(5221), 216-218.
- Svendsen, B., and T. J. Ahrens (1990), Shock-Induced Temperatures of CaMgSi₂O₆, *J. Geophys. Res.*, 95(B5), 6943-6953.
- Takei, H. (1978), Growth of fayalite (Fe₂SiO₄) single crystals by the floating-zone method, *Journal of Crystal Growth*, 43(4), 463-468.
- Tenner, T. J., R. A. Lange, and R. T. Downs (2007), The albite fusion curve re-examined: New experiments and the high-pressure density and compressibility of high albite and NaAlSi₃O₈ liquid, *American Mineralogist*, 92(10), 1573-1585.
- Ulmer, P., and R. Luth (1991), The graphite-COH fluid equilibrium in P, T, & fO₂ space, *Contributions to Mineralogy and Petrology*, 106(3), 265-272.
- Wicks, J. K., J. M. Jackson, and W. Sturhahn (2010), Very low sound velocities in iron-rich (Mg, Fe) O: Implications for the core-mantle boundary region, *Geophysical research letters*, 37(15), 15304.
- Williams, Q., J. Revenaugh, and E. J. Garnero (1998), A Correlation Between Ultra-Low Basal Velocities in the Mantle and Hot Spots, *Science*, 281(5376), 546-549.

TABLES

Table 1. Double-bob density measurements

T (K)	ρ g cm ⁻³	\pm
1551	3.710	0.002
1632	3.679	0.002
1723	3.652	0.002
1818	3.630	0.001

Table 2. Shock compression data

	Shot #	Flyer/ Driver	T (°C)	u_{fp} km s ⁻¹	±	u_p km s ⁻¹	±	U_s km s ⁻¹	±	ρ_H g cm ⁻³	±	P_H GPa	±
Chen et al. (2002)	999 ^a	Al2024/ Al2024	25	1.96	0.001	0.754	0.26	7.05	0.26	4.90	0.03	23.3	0.4
	1000 ^a	W/Al2024	25	2.03	0.01	1.51	0.18	6.95	0.18	5.61	0.05	46.2	0.9
	110	Cu/Cu	25	4.63	0.01	2.87	0.08	8.2	0.08	6.76	0.05	103.3	0.8
	120	Cu/Cu	25	5.30	0.002	3.29	0.08	8.71	0.08	7.00	0.06	124.7	0.8
	116	Ta/Ta	25	5.171	0.006	3.58	0.11	9.02	0.11	7.26	0.06	141.4	1.7
	113	Ta/Ta	25	5.38	0.005	3.69	0.17	9.44	0.17	7.21	0.1	153.0	2.1
	099	Ta/Ta	25	5.77	0.01	3.95	0.05	9.79	0.05	7.34	0.03	169.4	0.7
	107	Ta/Ta	25	6.25	0.001	4.27	0.1	10.15	0.1	7.59	0.07	190.5	1.5
	161	Ta/Ta	25	6.494	0.001	4.44	0.11	10.33	0.11	7.65	0.06	200.3	2.1
	126	Ta/Ta	25	6.51	0.005	4.57	0.1	10.57	0.1	7.73	0.08	211.9	1.6
This work	412	Ta/Ta	25	7.085	0.012	4.864	0.019	10.90	0.04	7.81	0.07	229.2	2.1
Chen et al. (2002)	995	Al2024/ Mo	1300	1.05	0.004	0.43	0.02	3.23	0.02	4.33	0.12	5.25	0.03
	996	Al2024/ Mo	1300	1.95	0.01	0.81	0.01	3.91	0.31	4.73	0.05	11.9	0.7
	981	Ta/Mo	1300	1.52	0.02	1.24	0.02	4.72	0.01	5.09	0.03	21.9	0.3
	993	Ta/Mo	1300	1.890	0.002	1.53	0.08	4.94	0.01	5.43	0.14	28.3	1.5
	990	Ta/Mo	1300	2.00	0.02	1.63	0.04	4.92	0.54	5.61	0.34	30.1	2.5
	994	Ta/Mo	1300	2.52	0.01	1.99	0.01	5.82	0.01	5.70	0.02	43.4	0.2
	998	W/Mo	1300	2.50	0.01	2.17	0.02	5.85	0.14	5.96	0.1	47.6	0.9
	This work	396	Ta/Mo	1299	4.997	0.003	3.82	0.003	8.45	0.03	6.76	0.02	119.5
	409	Ta/Mo	1300	6.050	0.002	4.58	0.01	9.50	0.05	7.15	0.04	161.0	0.6

^a40mm shots on Caltech polycrystalline fayalite

Table 3. Parameters used

	Units	Fe ₂ SiO ₄ liquid (1573 K)	Molybdenum ^d (1573 K)	Tantalum ^e (300 K)
$\Delta E_{tr} \approx \Delta H_{tr}$	kJ kg ⁻¹	-1584.2194 ^a	-	-
α	K ⁻¹	8.1949e-05 ^b	-	-
C_p	J kg ⁻¹ K ⁻¹	1182.35 ^c	-	-
C_v	J kg ⁻¹ K ⁻¹	1123.13 ^c	-	-
ρ_o	g cm ⁻³	-	9.96	16.65
C_o	km s ⁻¹	-	4.927	3.293
s		-	1.288	1.307

^aGhiorso and Sack [1995] ^bderived from this work, (see text and Table 1 for dV/dT) ^cLange and Navrotsky [1992] ^dAsimow et al. [2008] ^eMitchell and Nellis [1981]

Table 4. Equation of state fits for molten Fe₂SiO₄

	Units	SWEOS	SWEOS*	3BM/MG	4BM/MG	Source
T_o	K	1573	1573	1573	1573	
ρ_o	g cm ⁻³	3.699	3.699	3.699	3.699	this work
C_o	m s ⁻¹	2438±5	2670±8			AL04
s		1.58 ± 0.03	1.50±0.03			fitted
γ_o		0.412	0.412	0.412	0.412	derived
q		-1.45	-1.04	-0.95	-0.55	fitted
K_{oS}	GPa	21.99	26.38	21.99	21.99	derived
K_S'		5.33	4.99	7.28	6.64	fitted
K_S''	GPa ⁻¹				-0.47	fitted
χ^2				1.526	0.941	

SWEOS= shock wave equation of state. SWEOS*= shockwave EOS derived from the unconstrained linear fit (see text). 3BM/MG = 3rd order Birch-Murnaghan isentrope. 4BM/MG = 4th order Birch-Murnaghan isentrope. Sources: *Fitted* indicates an adjustable parameter, AL04 is Ai and Lange [2004]

Table 5. BM/MG fits for silicate liquid

	Units	Fo 4BM ^a	En 4BM ^b	An 4BM ^c	Di 3BM ^c	Source
T_o	K	1673	1673	1673	1673	
ρ_o	g cm^{-3}	2.825	2.618	2.584	2.643	LC90; L97
γ_o		0.816	0.365	0.18	0.49	LC90
q		-1.47	-1.71	-1.71 ^d	-1.28	fitted
K_S	GPa	42.19	24.66	20.39	24.57	derived
K_S'		4.73	9.18	2.31	6.98	derived
K_S'	GPa^{-1}	-0.11	-1.87	0.60		fitted
C_P	$\text{J K}^{-1} \text{kg}^{-1}$	1926.18	1761.15	1528.72	1612.56	LN92
C_V	$\text{J K}^{-1} \text{kg}^{-1}$	1684.30	1690.54	1512.56	1506.21	derived

^a corrected γ_o and refit to 4BM ^b from Mosenfelder *et al.* [2009] ^c resampled shock arrivals and refit to BM and excluding some shots, see text. ^d fixed q value LC90 is Lange and Carmichael [1990]; L97 is Lange [1997]; LN92 is Lange and Navrotsky [1992].

Table 6. Major oxide proportions for model mantle

	“chondrite” Andrault <i>et al.</i> (2011)	<i>KLB-1</i> Fiquet <i>et al.</i> (2010)	<i>KLB-1</i> Davis <i>et al.</i> (2010)
	mol %	mol %	mol %
CaO	2.6	1.5	2.8
MgO	45.9	53.7	50.8
Al ₂ O	1.8	1.2	1.8
SiO ₂	43.5	38.3	38.7
FeO	6.2	5.3	5.9
	mol %	mol %	mol %
Di	1.95	0.70	2.93
An	4.40	3.32	4.98
Fa	7.57	7.16	8.25
Fo	24.2	56.1	55.0
En	61.9	32.7	28.8

FIGURE CAPTIONS

Figure 1. A comparison of previous static sink/float and shock wave compression methods on fayalite liquid. The purple dashed line is an extrapolation of the 1773K isotherm from *Agee* [1992] with $K_T'=10.1$. The blue solid line is the fayalite liquid Hugoniot from *Chen et al.* [2002] with $K_S'=5.36$. Estimated shock temperatures are from *Chen et al.* [2002].

Figure 2. (a) Static image of the back of the molybdenum sample holder inverted 90 degrees clockwise such that the top is to the left. The centermost circle is the sample chamber or “top hat”; the guy wire posts are the smaller circles to the left and right. The vertical yellow lines correspond to the portion of the drivers (two outside lines) and the top hat (center line) that are sampled for shock wave arrival cutoffs. The bright vertical line is a superposed static image of the 25 micron slit in position. (b) On the streak image, the y-coordinate corresponds to position along the slit image in (a) where the x-coordinate is time increasing to the right. Yellow lines denote observed shock arrivals. Blue dashed lines are the 4th-order polynomial extrapolation of the shape of shock front from the drivers. The calibration streak shown at bottom converts an x-coordinate on the photo to a time during the experiment, giving the time between the shock wave passing from driver into sample (red line) and reaching the free surface of the top hat (rightmost yellow line). (c) An enlarged view of the top hat arrival with examples of pixel gray scale value vs. distance along the time axis profiles on the right. The arrival point is picked as the inflection point of the arc tangent function fit (black lines). The amplitude of the arctangent functions is arbitrary.

Figure 3. The double-bob density measurements between 1551 and 1831 K, plotted against temperature, are fit by the line $\rho(T) = 3699 \pm 1 - 0.30 \pm 0.01 * (T - 1573 \text{ K})$.

Figure 4. Density versus pressure diagram showing the new multi-anvil sink/float results for fayalite liquid at 1500°C. “Up” triangles represent observed floats, in which the fayalite liquid was denser than the mineral marker buoy. No sinks were accomplished in the new study. The green curve is the calculated compression for the spessartine garnet marker; the blue curve is the calculated compression for the almandine-rich garnet marker. Fayalite liquid density at 1-bar is from this study (purple diamond) determined by the Archimedean technique. The dashed and dotted curves are the compression curves calculated for fayalite liquid at 1500°C using the K from ultrasonic data [Ai and Lange, 2004] and the K' derived from the shock wave EOS and the 3rd-order Birch-Murnaghan EOS in this study, respectively (see Table 4). The thin purple solid curve is the compression curve for liquid fayalite from Agee [1992]. Float observations should plot below the correct liquid compression curve.

Figure 5. Preheated (1573K) fayalite Hugoniot in shock velocity (U_s)-particle velocity (u_p) space. Blue circles at the highest velocities were performed in this study. The red filled squares are taken from Chen *et al.* [2002] and were fit with the dotted blue line given in that study. The red solid line is the unconstrained un-weighted linear fit for all data points, and the light green solid line is the constrained un-weighted linear fit for all data points where the intercept is fixed at the bulk sound speed of liquid fayalite measured at 1573K. The hollow symbols are the initially solid experiments (300K) that were shocked to liquid from Chen *et al.* [2002] (hollow red

squares) and this work (hollow blue circle). The dashed green line represents a cold Hugoniot offset from the fitted hot liquid Hugoniot using the derived model for the liquid Grüneisen parameter.

Figure 6. The behavior of Grüneisen parameter for liquid and solid silicates with compression. The reference densities for the liquids (solid lines) are at 1673K for MgSiO_3 [Mosenfelder *et al.*, 2009] and Mg_2SiO_4 [Mosenfelder *et al.* 2009, corrected in this chapter] and at 1573 K for Fe_2SiO_4 (this study). The gamma functions for the solid materials are shown by dashed lines: magnesium perovskite (Pv) [Mosenfelder *et al.* 2009]-“BM3S model”; majorite (Mj) and enstatite (En) [Stixrude and Lithgow-Bertelloni, 2005].

Figure 7. Hugoniot data plotted in pressure-density space with thermal EOS fits for fayalite liquid and shock-melted single crystal all fixed at the Archimedean density at zero pressure. Data symbols are the same as Figure 5. Abbreviations: SWEOS- shock wave equation of state; BM/MG – Birch-Murnaghan/Mie-Grüneisen EOS; dKSFR- de Koker –Stixrude fundamental relation

Figure 8. Models for the early mantle upon cooling showing the comparison of the liquidus curves (black solid line) with the isentropic temperature profile (dotted line) of the same composition. (a) “Chondritic” composition and liquidus from Andraut *et al.* [2011]. (b) Peridotite KLB-1 composition and liquidus from Fiquet *et al.* [2010]. The critical isentrope with

its mantle potential temperature is shown in red. The EOS parameters used for En, Fo, An, and Di are given in Table 5 and Fa 3BM/MG parameters in Table 4. This figure is redone with the revised EOS in Chapter III Figure 8.

Figure 9. Calculated densities as function of pressure along a 10K/GPa mantle geotherm. The density at base of mantle (135 GPa) for each composition is thermally corrected from 3073K to 4400K (shaded cones). Also shown is the density profile from PREM [*Dziewonski and Anderson, 1981*] and the inferred density for a ULVZ from seismic reflection coefficients [*Rost et al. 2006*]. This figure is redone with the revised EOS in Chapter III Figure 9.

Figure 10. The density of liquid mixtures within En-Fs-Fo-Fa space at 135 GPa. The solids lines represent liquid mixtures that are neutrally buoyant with respect to solid magnesium perovskite (Pv) at different core-mantle-boundary temperatures from 3700-4500K. Any liquid compositions above these lines are less dense than Pv (white area) and any below are denser (blue striped area). Constant density lines for liquid compositions at 6.12 g/cc (dashed lines) represent the upper density limit for ULVZ's inferred from *Rost et al. [2006]*. The blue C represents the “chondrite” composition from used in *Andrault et al. [2011]*, and the yellow P is the peridotite composition from *Fiquet et al. [2010]*. Both compositions are given in Table 6. The gray arrows indicate the direction of liquid composition change with fractional crystallization of Pv (disregarding partitioning of Fe). a) The EOS parameters used for En and Fo are given in Table 5 and Fa 3BM parameters in Table 4. b) The EOS parameters used for En and Fa are given in Table 4 and Fo 3BM parameters in Table 3 of Chapter III.

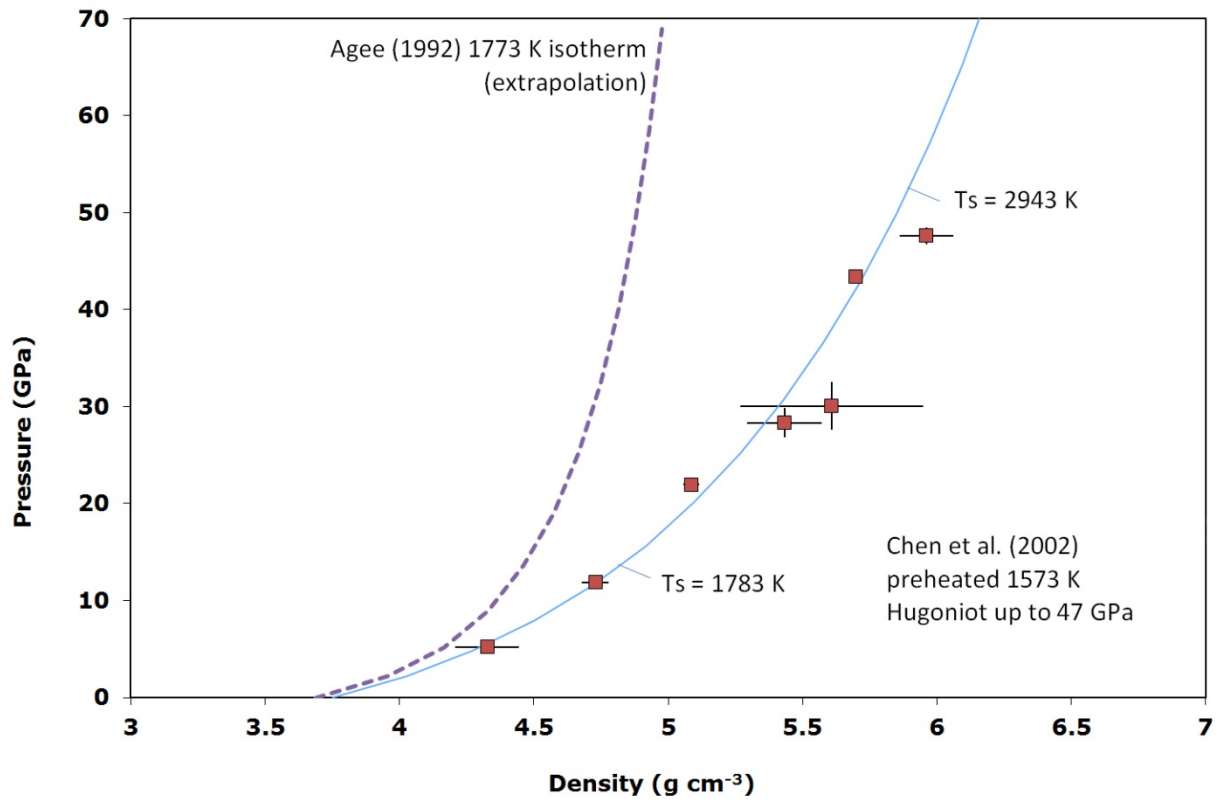


Figure 1

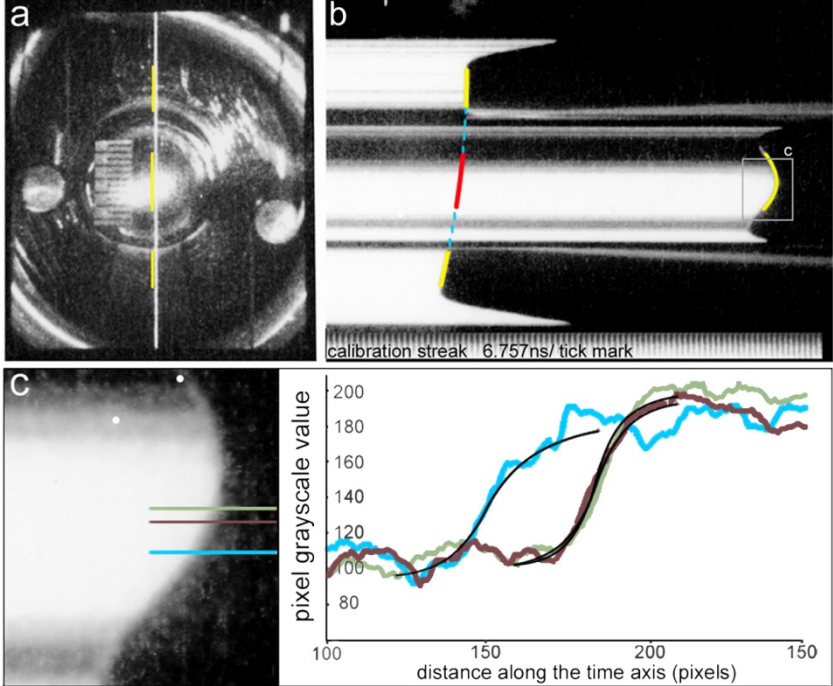


Figure 2

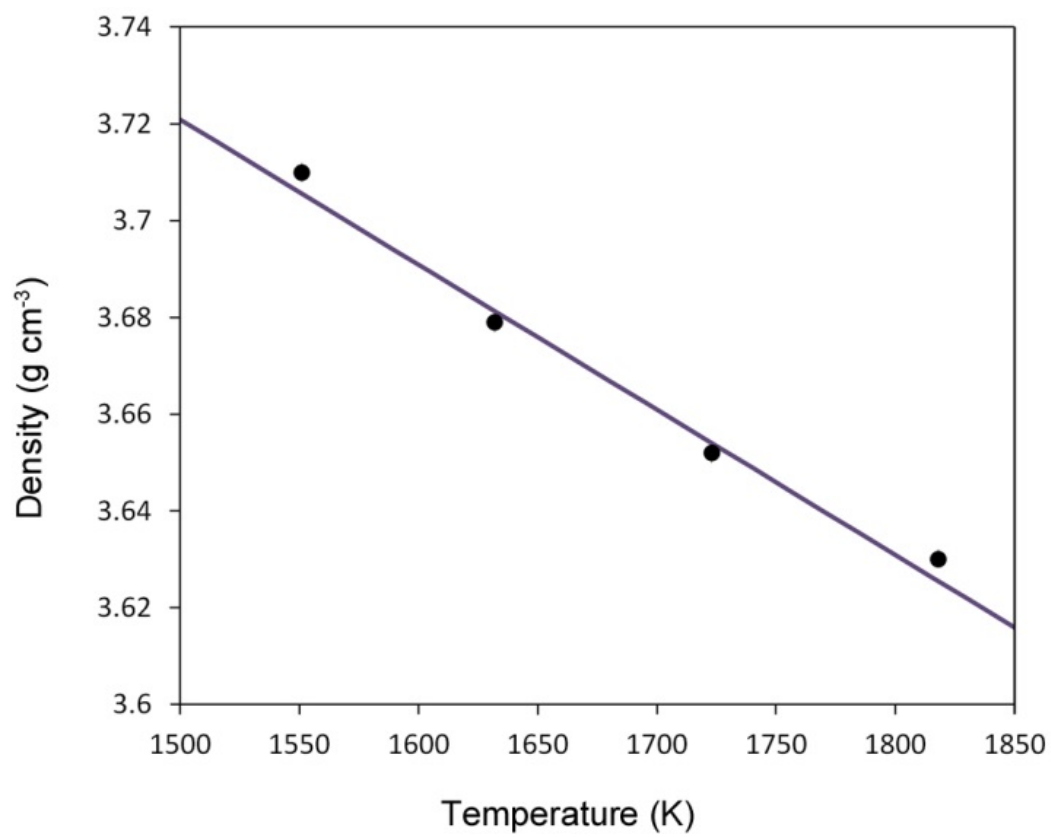


Figure 3

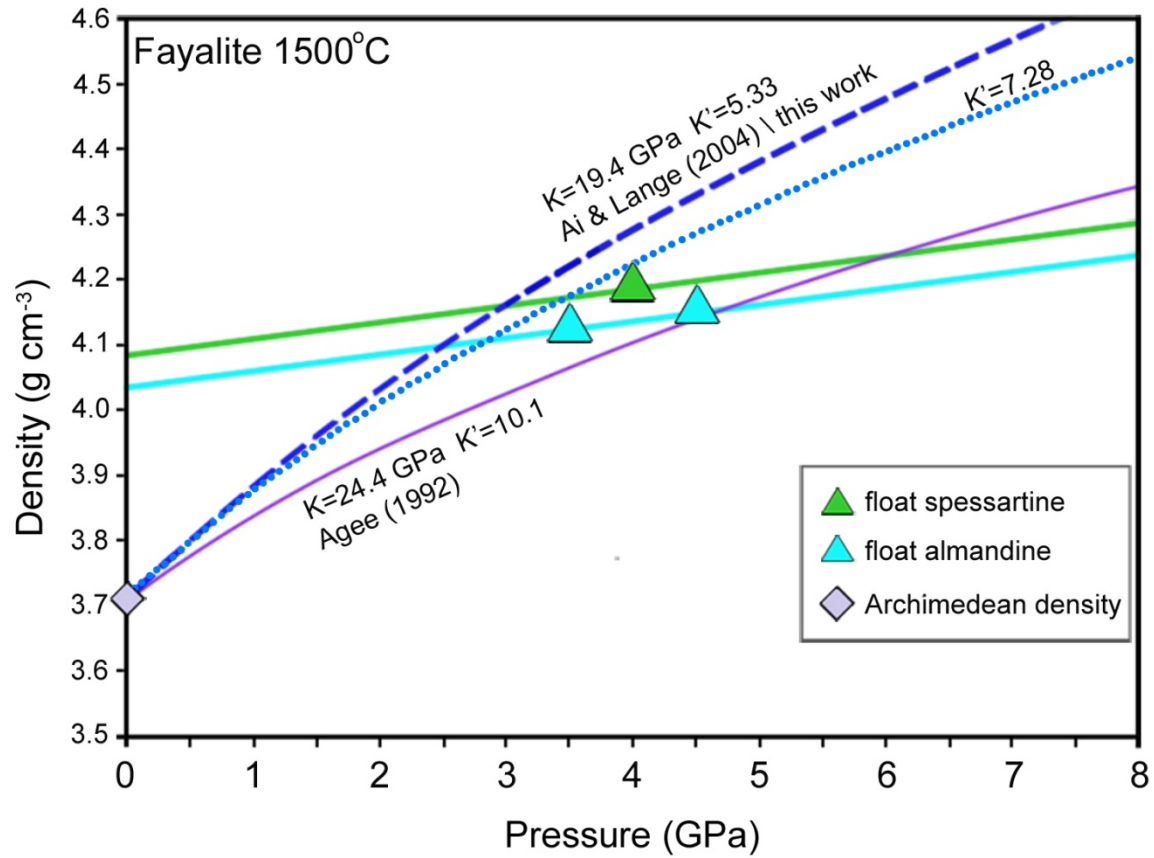


Figure 4

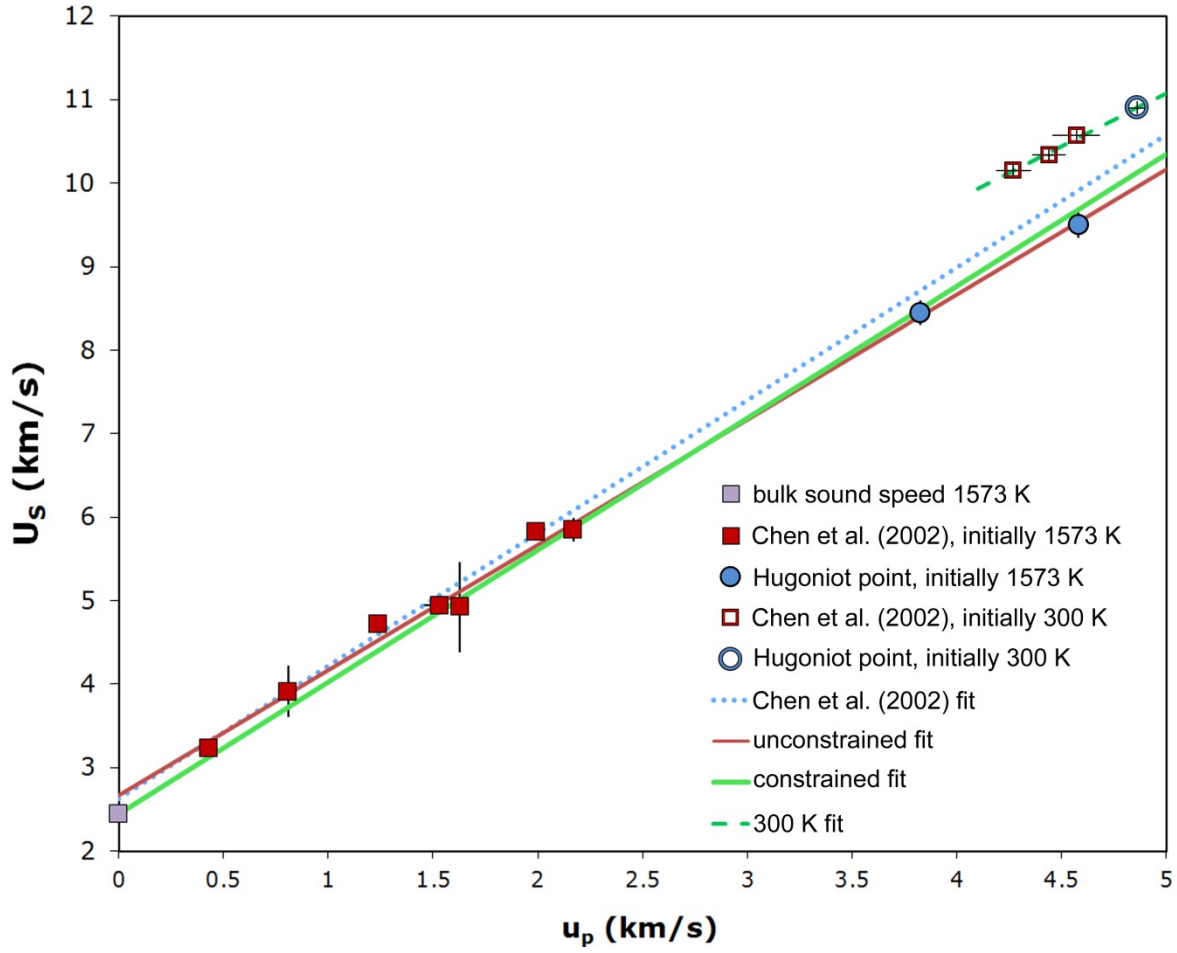


Figure 5

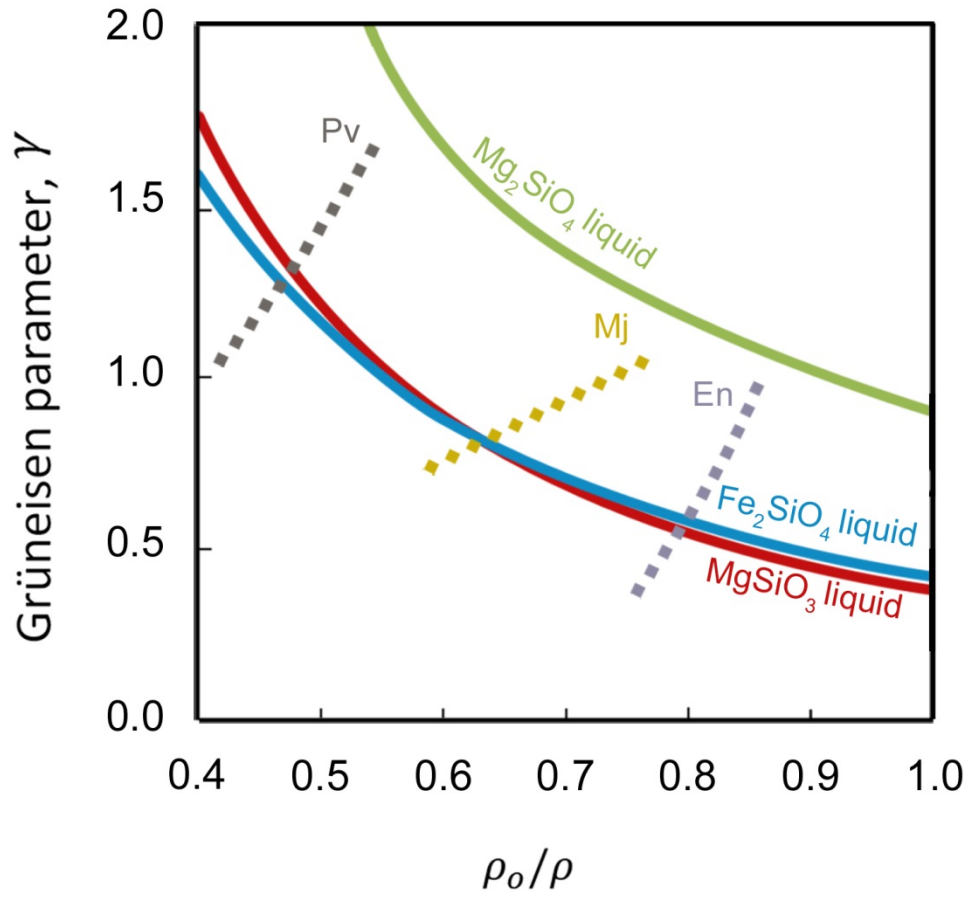


Figure 6

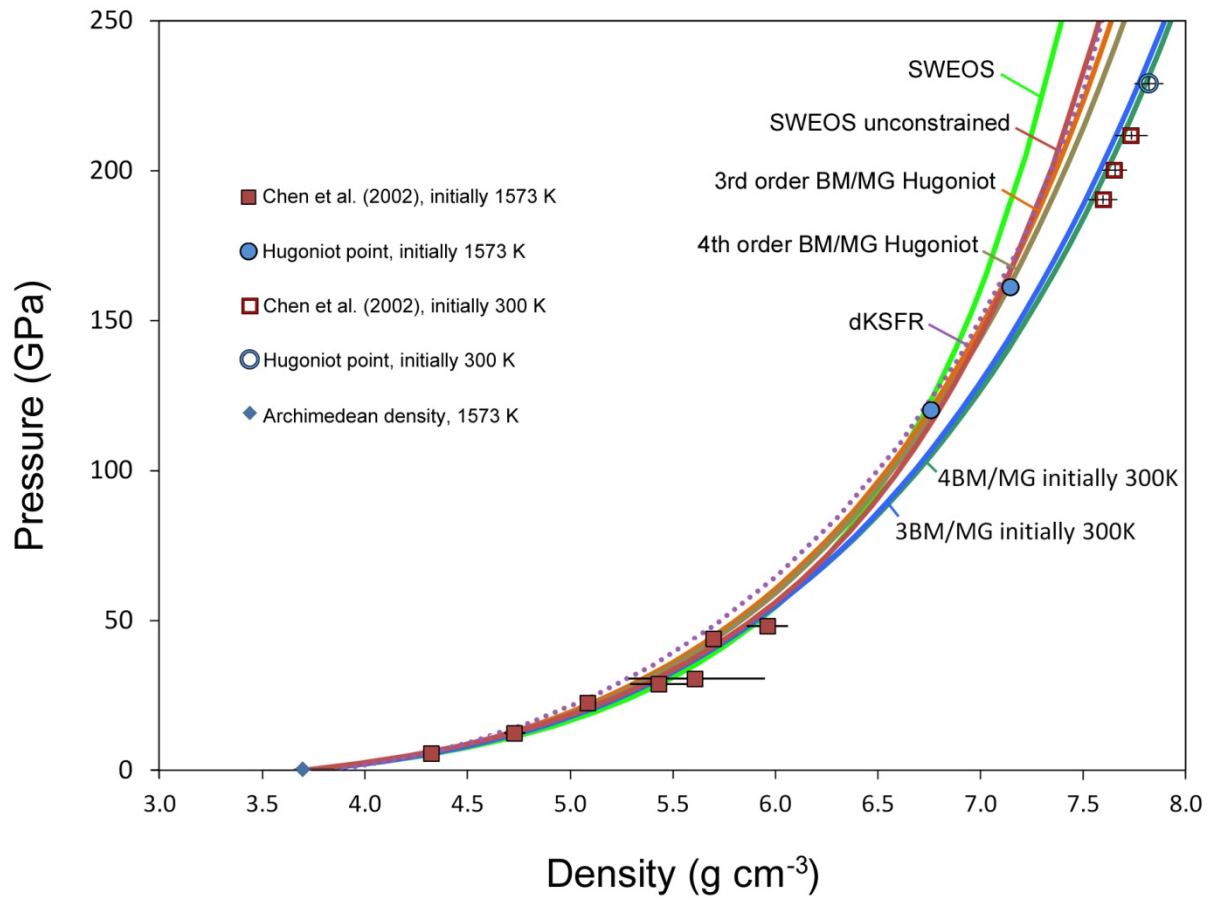


Figure 7

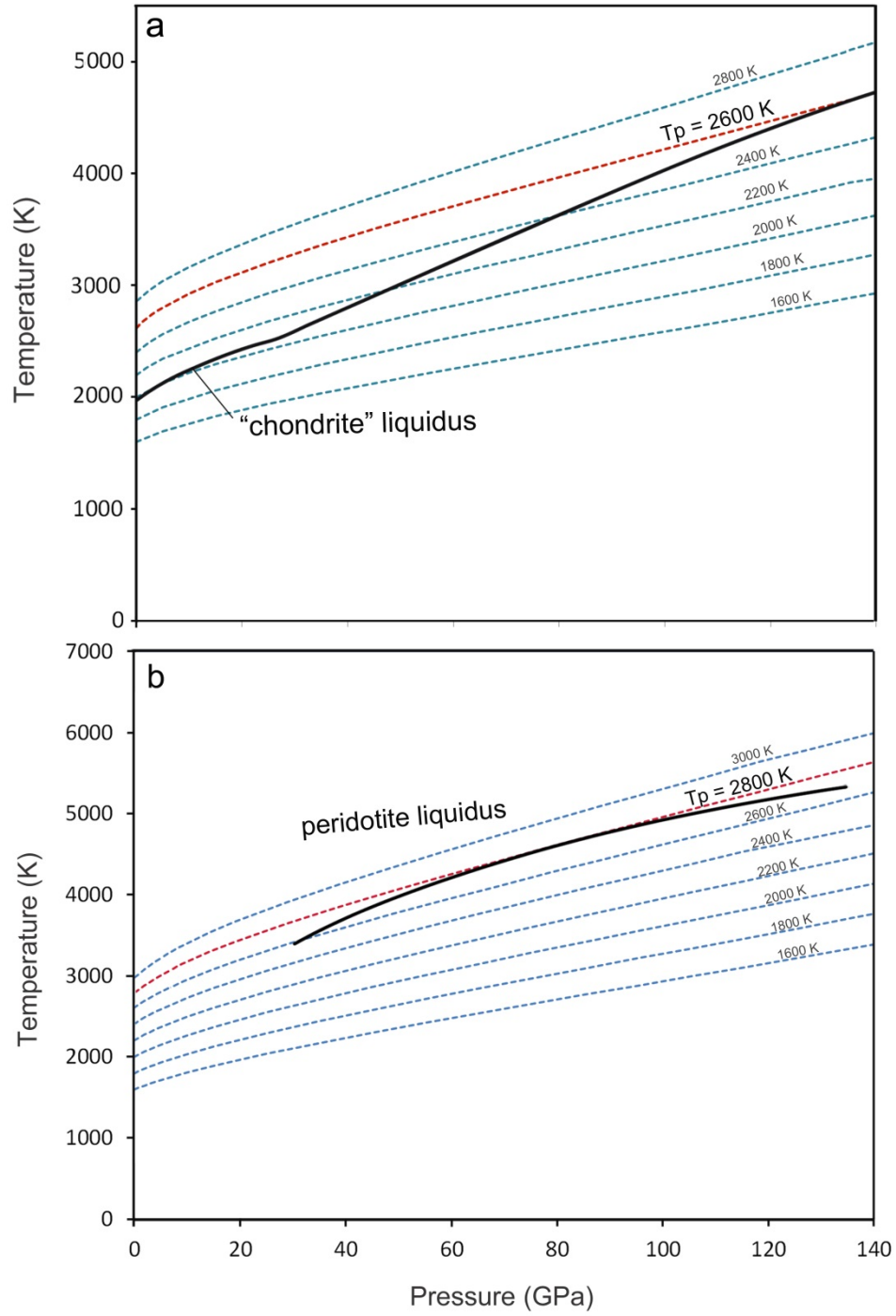


Figure 8

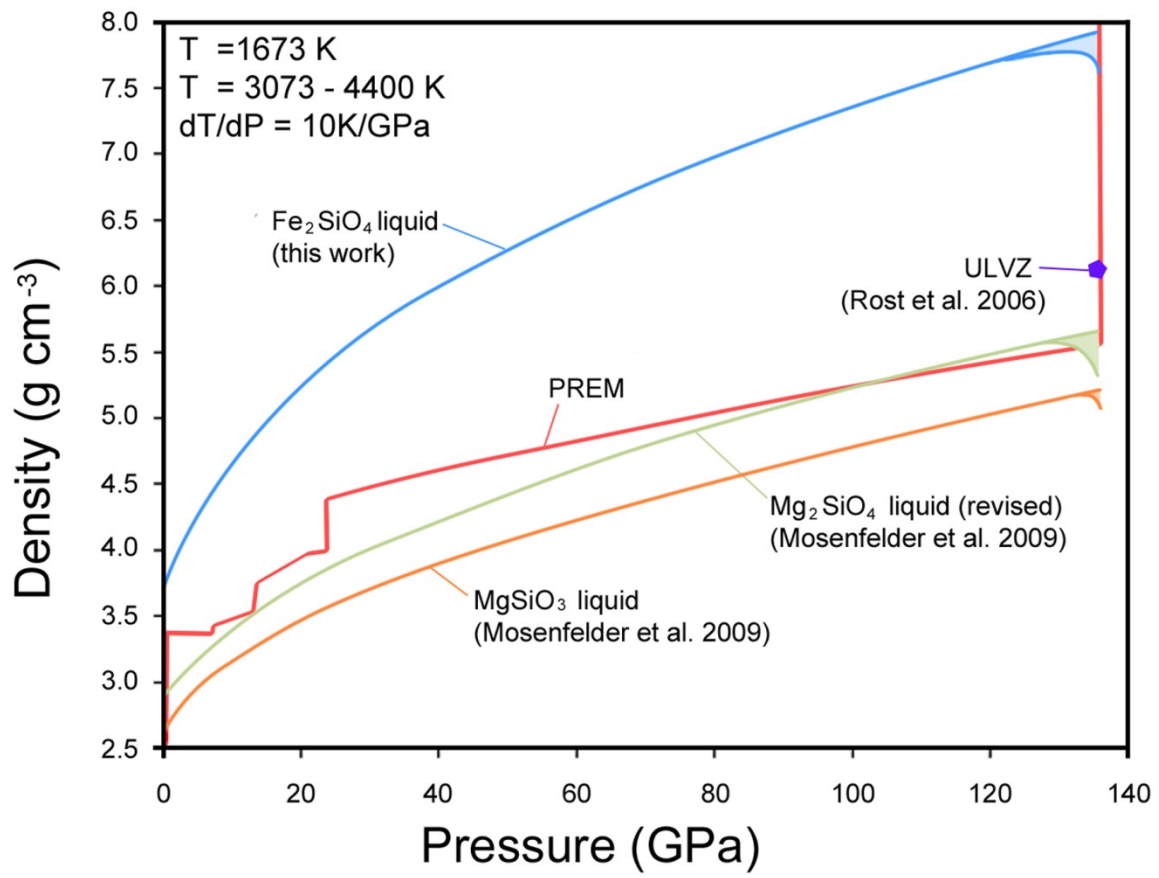


Figure 9

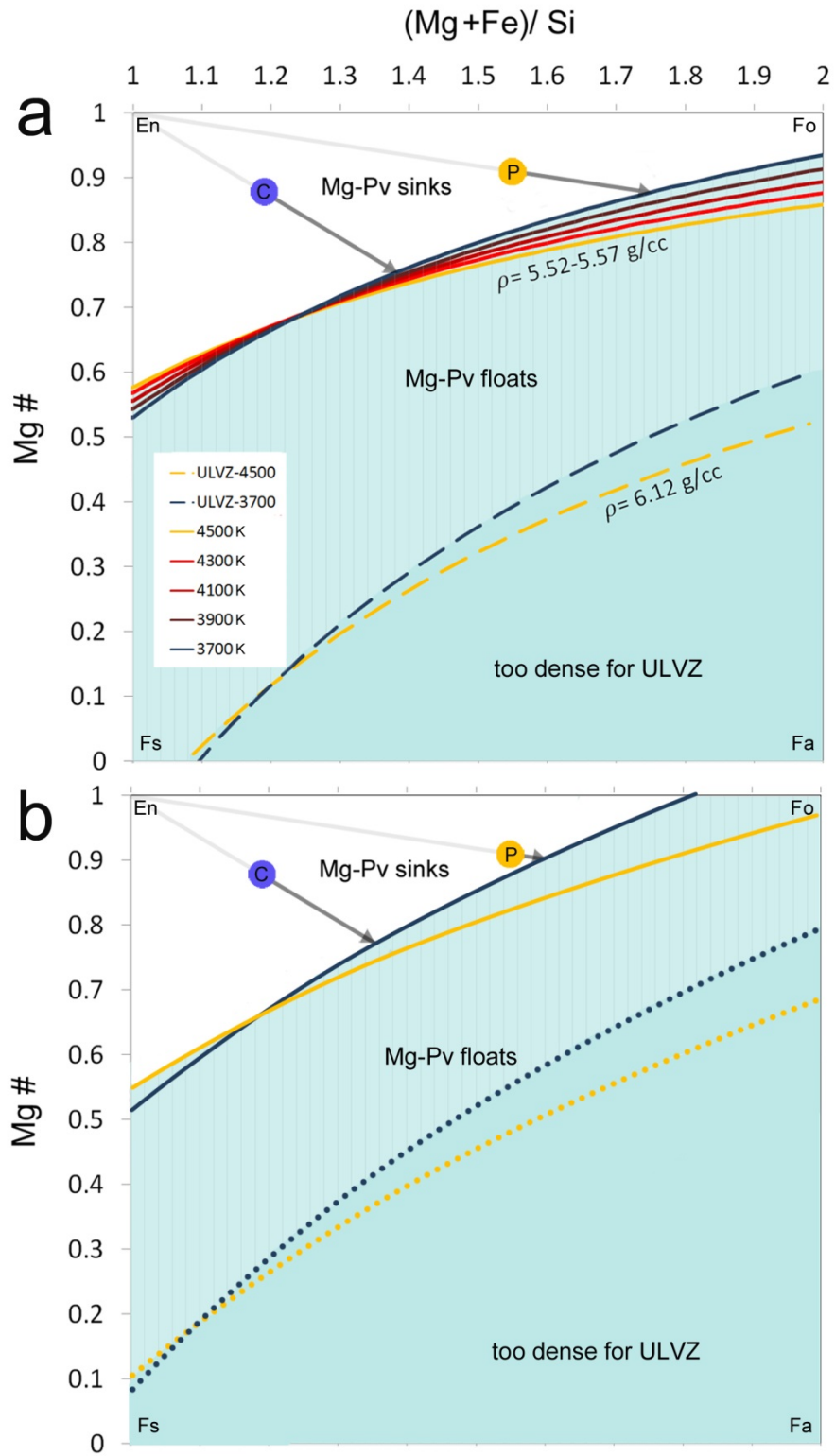


Figure 10